LBL-14373

Lawrence Berkeley Laboratory
UNIVERSITY OF CALIFORNIA

Materials & Molecular Research Division

RECEIVED
LAWRENCE
BERKELEY LABORATORY

MAY 28 1982

LIBRARY AND
DOCUMENTS SECTION

COHERENT RAYLEIGH-BRILLOUIN SPECTROSCOPY

Alexander Gerson Jacobson
(Ph.D. thesis)

April 1982

TWO-WEEK LOAN COPY

This is a Library Circulating Copy which may be borrowed for two weeks. For a personal retention copy, call Tech. Info. Division, Ext. 6782.

LBL-14373 c.2

Prepared for the U.S. Department of Energy under Contract DE-AC03-76SF00098

DISCLAIMER

This document was prepared as an account of work sponsored by the United States Government. While this document is believed to contain correct information, neither the United States Government nor any agency thereof, nor the Regents of the University of California, nor any of their employees, makes any warranty, express or implied, or assumes any legal responsibility for the accuracy, completeness, or usefulness of any information, apparatus, product, or process disclosed, or represents that its use would not infringe privately owned rights. Reference herein to any specific commercial product, process, or service by its trade name, trademark, manufacturer, or otherwise, does not necessarily constitute or imply its endorsement, recommendation, or favoring by the United States Government or any agency thereof, or the Regents of the University of California. The views and opinions of authors expressed herein do not necessarily state or reflect those of the United States Government or any agency thereof or the Regents of the University of California.

LBL-14373

COHERENT RAYLEIGH-BRILLOUIN SPECTROSCOPY

Alexander Gerson Jacobson

Ph.D. Thesis

April 1982

Materials and Molecular Research Division
Lawrence Berkeley Laboratory
University of California
Berkeley, CA 94720

This work was supported by the Director, Office of Energy Research, Office of Basic Energy Sciences, Materials Sciences Division of the U.S. Department of Energy under Contract Number DE-AC03-76SF00098.

Alexander Gerson Jacobson

Coherent Rayleigh-Brillouin Spectroscopy

ABSTRACT

Nonlinear optical spectroscopic techniques have been extended to the Rayleigh-Brillouin region of the light scattering spectrum by studying the dispersion and polarization dependence of the optical Kerr effect, governed by $\chi^{(3)}(\omega = \omega + \Omega - \Omega)$.

As $|\omega - \Omega|$ is tuned through zero in liquid CS_2, two distinct resonant behaviors are observed. First, in a broad region extending a few wavenumbers about zero detuning there is a resonance due to optical-field-induced molecular reorientation. Analysis of the spectrum enabled the determination of the reorientation time of CS_2, 2.0 psec. The polarization dependence of the reorientational signal agrees with theoretical predictions. We have thus demonstrated "Coherent Rayleigh-wing Spectroscopy."

Second, by tuning the lasers to the acoustic phonon resonance at $|\Omega - \omega| = .23\ cm^{-1}$, we observe the Brillouin spectrum. This appears as an assymmetric doublet superimposed on the "Rayleigh-wing" background. The intensity dependence of the doublet is explained by a large signal treatment of the nonlinear optical process. We demonstrated, both theoretically and experimentally, the smooth transformation of the spectrum from the parametric limit, where the signal is proportional to $|\chi^{(3)}|^2$, to a region where Stokes gain and anti-Stokes loss become evident. Thus we have demonstrated the dispersion and intensity dependence of "Coherent Brillouin Spectroscopy."

To overcome the experimental limitations of this study, we recommend Raman gain measurements be used for obtaining the absolute light scattering cross sections of material. In future investigations, it should be possible to measure the absolute Raman, electronic, Brillouin, and orientational contributions to the nonlinear susceptibility with high precision. A series of such measurements could then accurately quantify the light scattering parameters of standard samples.

Finally, we study the dispersion of Brillouin-induced phase-conjugate wave generation. In a small-signal analysis, we predict the unique resonant properties of the "Brillouin Mirror" created by the enhancement of conjugate wave generation at the acoustic phonon resonances. By controlling the pump beam polarization, it is possible to control the apportionment of resonant reflectivity at two distinct Brillouin shifts. Thus the Brillouin nonlinearity may be used to construct a polarization tunable, phase conjugate resonant reflector.

ACKNOWLEDGEMENT

I would like to thank Ron Shen for having me as his student and placing great emphasis on fundamentals and clarity of deduction. Eric Hanson was instrumental in getting me started in the laboratory and suggested studying this topic. Melvin Magliocco taught me the basics of mechanical design and greatly helped in the apparatus construction phase. Many students, including especially Robert Smith and Jack Feinberg, provided the feeling of mutual purpose and commitment so helpful during midnight experimentation. Rita Jones and Sumner Davis helped put this experience in a larger perspective, an act of great kindness. Finally, I wish to thank Clyde Thom for his friendship and example.

This work was supported by the Director, Office of Energy Research, Office of Basic Energy Sciences, Materials Sciences Division of the U.S. Department of Energy under Contract Number DE-AC03-76SF00098.

TABLE OF CONTENTS

Page

1. Rayleigh, Brillouin, and Electronic Contributions to $\chi^{(3)}$. 1
2. Coherent Raman Spectroscopy. 25
3. The Experimental Apparatus. 46
4. Results, Interpretation, and Suggestions for Future Work. 70
5. A Tunable "Brillouin Mirror". 90

References. 102

1. RAYLEIGH, BRILLOUIN, AND ELECTRONIC CONTRIBUTIONS TO $\chi^{(3)}$

1.1 INTRODUCTION

Nonlinear optical effects due to optical-field-induced molecular reorientation and acoustic phonon excitation have been known almost as long as research workers have studied laser-matter interactions. Intensity-dependent index of refraction change due to optical beams was recognized as a generalization of the DC Kerr effect early in the development of nonlinear optics.[1] Gires and Mayer observed the "optical Kerr effect" due to optical-field-induced linear birefringence;[2] Maker, Terhune, and Savage observed the rotation of the polarization ellipse due to circular birefringence.[3] The intensity-dependent index of refraction can lead to the self-focusing of an optical beam, as first discussed by Askaryan,[4] and by Chiao et al.[5] Stimulated Rayleigh-wing scattering was investigated by Mash et al.[6] Finally, Bloembergen and Lallemand identified the optical Kerr mechanism for the spectral broadening of stimulated Raman lines under conditions where self-focusing, stimulated Raman scattering, and stimulated Rayleigh-wing scattering were all taking place during the same laser pulse.[7]

Meanwhile the phenomenon of stimulated Brillouin scattering was discovered by Chiao et al.[5,8] It was recognized then that electrostriction could also lead to a nonlinear refractive index change. The relative magnitude of the optical Kerr and electrostrictive contributions to the nonlinear index was discussed by Shen.[9]

In the period of 1966-72, experimental techniques for the study of nonlinear optical effects became more refined. A great wealth of quantitative data began to be accumulated on the resonance frequencies,

strengths, and lineshapes of both spontaneous and stimulated scattering processes in various materials. In this period the laser became a standard research tool and spontaneous light scattering methods diffused into a number of branches of analytical science. A survey of the stimulated light scattering field during this period is given in reference 10.

Post 1972, nonlinear optics entered a third phase and became more mature. Stimulated scattering processes began to be used as analytical tools, known generally as "Coherent Raman Spectroscopy." In all coherent Raman techniques, a tunable laser scans through the Raman resonance. In the first experiments,[11] performed by Maker and Terhune in 1964, stimulated Raman scattering in various liquids with a pump ruby laser was used as the "tunable laser." The experiments being performed today are possible only because of the development and proliferation of the tunable dye laser. A plethora of techniques have been developed — these will be reviewed in Chapter 2.

Our aim in the present investigation was twofold. We wanted to show that as an extension of coherent Raman spectroscopy, coherent Brillouin and Rayleigh-wing spectroscopy were also possible, and thus prove the viability of nonlinear spectroscopic techniques in the low-frequency region of the light scattering spectrum. And we were challenged to solve the experimental problems associated with detecting a weak nonlinear signal in the presence of intense noise sources at closely adjacent spatial and temporal frequencies.

We begin this dissertation with a general discussion of the nonlinear susceptibility tensor, followed by a derivation of the nonlinearities associated with the Rayleigh and Brillouin mechanisms.

1.2 THE OPTICAL SUSCEPTIBILITY TENSORS[11,12]

In the spirit of perturbation theory, we suppose that the polarization of a material may be expanded into a power series in terms of the local electric field strength. We can write in general,

$$\vec{P}(\vec{r},t) = \vec{P}^{(1)}(\vec{r},t) + \vec{P}^{(2)}(\vec{r},t) + \vec{P}^{(3)}(\vec{r},t) + --- + \vec{P}^{(n)}(\vec{r},t) \quad (1.1)$$

where

$$P_i^{(1)}(\vec{r},t) = \int d^3r_1 dt_1 \chi_{ij}^{(1)}(\vec{r}_1,t_1) E_j(\vec{r} - \vec{r}_1, t - t_1) \quad (1.2a)$$

$$P_i^{(2)}(\vec{r},t) = \int d^3r_1 d^3r_2 dt_1 dt_2 \chi_{ijk}^{(2)}(\vec{r}_1,t_1;\vec{r}_2,t_2)$$

$$\times E_j(\vec{r} - \vec{r}_1, t - t_1) E_k(\vec{r} - \vec{r}_2, t - t_2) \quad (1.2b)$$

$$P_i^{(3)}(\vec{r},t) = \int d^3r_1 d^3r_2 d^3r_3 dt_1 dt_2 dt_3 \chi_{ijk\ell}^{(3)}(\vec{r}_1,t_1;\vec{r}_2,t_2;\vec{r}_3,t_3)$$

$$\times E_j(\vec{r} - \vec{r}_1, t - t_1) E_k(\vec{r} - \vec{r}_2, t - t_2) E_\ell(\vec{r} - \vec{r}_3, t - t_3) \quad (1.2c)$$

and so on. Here $\chi^{(1)}$, $\chi^{(2)}$, and $\chi^{(3)}$ are the first, second, and third-order response functions of the medium to the electric field. The subindices of the χ's are associated, in order, with the spatial coordinates. For monochromatic (laser) waves, with the help of the Fourier transform pair

$$\vec{E}(\vec{r},t) = \int d^3k d\omega \vec{E}(\vec{k},\omega) e^{i(\vec{k}\cdot\vec{r}-\omega t)} \quad (1.3a)$$

$$\vec{E}(\vec{k},\omega) = \frac{1}{(2\pi)^4}\int d^3r dt \vec{E}(\vec{r},t)e^{-i(\vec{k}\cdot\vec{r}-\omega t)} \tag{1.3b}$$

we obtain

$$P_i^{(1)}(\vec{k},\omega) = \chi_{ij}(\vec{k},\omega)E_j(\vec{k},\omega) \tag{1.4a}$$

$$P_i^{(2)}(\vec{k},\omega) = \chi_{ijk}(\vec{k} = \vec{k}_1 + \vec{k}_2;\omega = \omega_1 + \omega_2)E_j(\vec{k}_1,\omega_1)E_k(\vec{k}_2,\omega_2) \tag{1.4b}$$

$$P_i^{(3)}(\vec{k},\omega) = \chi_{ijk\ell}(\vec{k} = \vec{k}_1 + \vec{k}_2 + \vec{k}_3;\omega = \omega_1 + \omega_2 + \omega_3)$$

$$\times\ E_j(\vec{k}_1,\omega_1)E_k(\vec{k}_2,\omega_2)E_\ell(\vec{k}_3,\omega_3) \tag{1.4c}$$

where

$$\chi_{ij}^{(1)}(\vec{k},\omega) = \int d^3r_1 dt_1 \chi_{ij}^{(1)}(\vec{r}_1,t_1)e^{-i(\vec{k}_1\cdot\vec{r}_1-\omega_1 t_1)} \tag{1.5a}$$

$$\chi_{ijk}^{(2)}(\vec{k},\omega) = \int d^3r_1 dt_1 d^3r_2 dt_2 \chi_{ijk}^{(2)}(\vec{r}_1,t_1;\vec{r}_2,t_2)\exp - i(\vec{k}_1\cdot\vec{r}_1 + \vec{k}_2\cdot\vec{r}_2$$

$$- \omega_1 t_1 - \omega_2 t_2) \tag{1.5b}$$

$$\chi_{ijk\ell}^{(3)}(\vec{k},\omega) = \int d^3r_1 dt_1 d^3r_2 dt_2 d^3r_3 dt_3 \chi_{ijk\ell}(\vec{r}_1,t_1;\vec{r}_2,t_2;\vec{r}_3,t_3)$$

$$\times \exp - i(\vec{k}_1\cdot\vec{r}_1 + \vec{k}_2\cdot\vec{r}_2 + \vec{k}_3\cdot\vec{r}_3 - \omega_1 t - \omega_2 t_2 - \omega_3 t_3). \tag{1.5c}$$

For isotropic media, the symmetry consideration leads to:[13]

$$\chi_{ij}^{(1)}(\vec{k},\omega) = \chi(\vec{k},\omega)\delta_{ij} \tag{1.6a}$$

$$\chi^{(2)}_{ijk}(\vec{k},\omega) = 0 \tag{1.6b}$$

$$\chi^{(3)}_{ijk\ell}(\vec{k},\omega) = \chi_{1122}\delta_{ij}\delta_{k\ell} + \chi_{1212}\delta_{ik}\delta_{j\ell} + \chi_{1221}\delta_{i\ell}\delta_{jk}. \tag{1.6c}$$

In the following, we will focus on the third-order nonlinear susceptibility.

Maker and Terhune suggested the following convention, which has often been adopted in the literature.[11,14]

$$P^{(3)}_i(\vec{k},\omega) = D\chi_{ijk\ell}(\vec{k} = \vec{k}_a + \vec{k}_b + \vec{k}_c;\omega = \omega_a + \omega_b + \omega_c)$$

$$\times\ E_j(\vec{k}_a,\omega_a)E_k(\vec{k}_b,\omega_b)E_\ell(\vec{k}_c,\omega_c) \tag{1.7}$$

where D = 6 if the frequencies a, b, and c are distinct, D = 3 if two of them are equal, and D = 1 if they are all the same. Sometimes, a monochromatic field is written as

$$\vec{E} = \tfrac{1}{2}\vec{E}'(\vec{k},\omega)e^{i(\vec{k}\cdot\vec{r}-\omega t)} + \text{c.c.} \tag{1.8}$$

and correspondingly,

$$\vec{P}^{(n)} = \tfrac{1}{2}\vec{P}'^{(n)}(\vec{k},\omega)e^{i(\vec{k}\cdot\vec{r}-\omega t)} + \text{c.c.} \tag{1.9}$$

A new susceptibility is defined by the relation

$$P'^{(3)}_i(\vec{k},\omega) = D\chi'_{ijk\ell}(\vec{k},\omega)E'_j(\vec{k}_a,\omega_a)E'_k(\vec{k}_b,\omega_b)E'_\ell(\vec{k}_c,\omega_c). \tag{1.10}$$

On the other hand, (1.7) yields

$$\tfrac{1}{2}P_i'^{(3)}(\vec{k},\omega) = \frac{1}{8}\, D\chi^{(3)}_{ijk\ell}(\vec{k},\omega)E_j'(\vec{k}_a,\omega_a)E_k'(\vec{k}_b,\omega_b)E_\ell'(\vec{k}_c,\omega_c). \qquad (1.11)$$

Comparison of (1.10) and (1.11) gives

$$\chi_{ijk\ell}'^{(3)} = \tfrac{1}{4}\chi^{(3)}_{ijk\ell}. \qquad (1.12)$$

We will use $\chi_{ijk\ell}'^{(3)}$ in the following discussion.

1.3 THE NONLINEAR SUSCEPTIBILITY DUE TO OPTICAL-FIELD-INDUCED MOLECULAR REORIENTATION[6,14-16]

Consider an axially symmetric molecule with symmetry axis $\hat{t}$ oriented with polar angles (θ,ϕ), Fig. 1.1. Let the molecular polarizability be α_2 along the symmetry axis and α_1 perpendicular to it. If an electric field is now applied, we have

$$\vec{p} = \alpha_1\vec{E} + (\alpha_2 - \alpha_1)\hat{t}(\hat{t}\cdot\vec{E})$$

$$= \overleftrightarrow{\alpha}(\theta,\phi)\cdot\vec{E}. \qquad (1.13)$$

In the coordinate system of Fig. 1.1, the $\overleftrightarrow{\alpha}(\theta,\phi)$ tensor works out to be

$$\overleftrightarrow{\alpha}(\theta,\phi) = \begin{pmatrix} \alpha_1 + \Delta\alpha\sin^2\theta\cos^2\phi & \Delta\alpha\sin^2\theta\sin\phi\cos\phi & \Delta\alpha\sin\theta\cos\theta\cos\phi \\ \Delta\alpha\sin^2\theta\sin\phi\cos\phi & \alpha_1 + \Delta\alpha\sin^2\theta\sin^2\phi & \Delta\alpha\sin\theta\cos\theta\sin\phi \\ \Delta\alpha\sin\theta\cos\theta\cos\phi & \Delta\alpha\sin\theta\cos\theta\sin\phi & \alpha_1 + \Delta\alpha\cos^2\theta \end{pmatrix} \qquad (1.14)$$

where $\Delta\alpha = \alpha_2 - \alpha_1$. The energy needed to change the dipole moment an amount $d\vec{p}$ is the sum of the work needed to polarize the molecule and the change in energy of the dipole in the field

$$dU = \vec{E} \cdot d\vec{p} + d(-\vec{p} \cdot \vec{E}) = -\vec{p} \cdot d\vec{E}. \tag{1.15}$$

Thus

$$U(\theta) = -\int \overleftrightarrow{\alpha}(\theta,\phi):\vec{E}d\vec{E} = -\tfrac{1}{2}\alpha_{ij}(\theta)E_iE_j \tag{1.16}$$

where $\alpha_{ij}(\theta)$ now stands for (1.14). For an ensemble of molecules, the equilibrium field-dependent distribution function is

$$f_{eq}(\theta,t) = \exp[-U(\theta)/kT]/\int d\Omega\exp[-U(\theta)/kT]. \tag{1.17}$$

This is explicitly time dependent through the time dependence of E_iE_j in $U(\theta)$, and is maximized when the molecule's axis of easy polarizability lies along the instantaneous electric field. To first order in U, (1.17) becomes

$$f_{eq}(\theta,t) = \tfrac{1}{4}\pi[1 + 1/kT(\overline{U(\theta)} - U(\theta))] \tag{1.18}$$

where $\overline{}$ stands for angular average $\int d\Omega/4\pi$. That it is sufficient to work with the first order expansion (1.18) may be justified as follows. For a polarizability $\alpha \sim 10^{-23}$ cm^3, the laser intensity ~ 2 GW/cm^2 (the largest encountered in our experiments), $U/kT \sim 10^{-3}$. Performing the average in (1.18) we obtain

$$f_{eq}(\theta,t) = \frac{1}{4\pi}\left[1 + \frac{1}{2kT}(\alpha_{ij}(\theta) - \alpha\delta_{ij})E_iE_j\right] \tag{1.19}$$

where α is the average polarizability

$$\alpha = 1/3(2\alpha_1 + \alpha_2). \tag{1.20}$$

The field-dependent equilibrium distribution function f_{eq} acts as the driving force for the instaneous distribution function $f(\theta,t)$. We have

$$\tau \frac{\partial f}{\partial t} + f = f_{eq}. \tag{1.21}$$

The assumption (1.21) that $f(\theta,t)$ relaxes toward $f_{eq}(\theta,t)$ with a single time constant τ is Debye's analysis of the reorientation of a polar molecule in a fluid.[17] In this model, the torque on the molecule due to a linearly polarized applied field drives the distribution function and is opposed by viscous damping. The relaxation time is given by

$$\tau' = 3V\eta/kT \tag{1.22}$$

where V is an effective molecular volume and η is the viscosity. For an induced, rather than permanent dipole, modification of the theory reduces the expected value of the relaxation time by a factor of one-third:[14]

$$\tau = 1/3\tau' = V\eta/kT. \tag{1.23}$$

As we will see, the assumption that the molecular dynamics are described by (1.21) leads to a Lorentzian frequency dependence for the nonlinear susceptibility. The experiment must be designed to test the expected shape of the dispersion curve and then extract a value for the relaxation time.

Using (1.19) and (1.21) we may solve for the time dependent distribution function. We obtain

$$f(\theta,t) = \tfrac{1}{4}\pi\left\{1 + \frac{1}{2kT}\,(\alpha_{ij}(\theta) - \alpha_{ij}) \int_{-\infty}^{t} \rho(t - t')E_i(t')E_j(t')dt'\right\}, \tag{1.24}$$

$$\rho(t - t') = \tau^{-1}\exp[-\,(t - t')/\tau]. \tag{1.25}$$

Using this distribution function, we calculate the expected value of the polarizability $\langle\alpha_{ij}(\theta,t)\rangle$ and the dipole moment per unit volume, separating the latter into the linear and nonlinear polarizations:

$$\begin{aligned}\langle\alpha_{ij}(\theta,t)\rangle &= \int d\Omega\alpha_{ij}(\theta)f(\theta,t)\\ &= \alpha\delta_{ij} + \tfrac{1}{2}kT\left\{\left(\overline{\alpha_{ij}\alpha_{k\ell}} - \alpha^2\delta_{ij}\delta_{k\ell}\right)\right.\\ &\qquad\left.\times\int_{-\infty}^{t}\rho(t - t')E_k(t')E_\ell(t')dt'\right\}\end{aligned} \tag{1.26}$$

$$P_i(t) \equiv N\ \langle\alpha_{ij}(\theta,t)\rangle\ E_j(t) \equiv P_i^{(1)}(t) + P_i^{(3)}(t). \tag{1.27}$$

The linear polarization is given by

$$P_i^{(1)}(t) = N\alpha E_i(t), \tag{1.28}$$

the expected result for an unperturbed, isotropic fluid. The nonlinear polarization is given by

$$P_i^{(3)}(t) = \int_{-\infty}^{t} a(t - t')[E^2(t')]E_i(t)dt'$$

$$+ \int_{-\infty}^{t} b(t - t')[\vec{E}(t') \cdot \vec{E}(t)]E_i(t')dt' \qquad (1.29)$$

where

$$b(t) = - 3a(t) = \frac{N(\alpha_2 - \alpha_1)^2}{15kT} \rho(t). \qquad (1.30)$$

In deriving (1.29), we made use of the angular average

$$\left(\overline{\alpha_{ij}\alpha_{k\ell}} - \alpha^2\delta_{ij}\delta_{k\ell}\right) = 2/45(\alpha_2 - \alpha_1)^2$$

$$\times [3/2(\delta_{ik}\delta_{j\ell} + \delta_{i\ell}\delta_{jk}) - \delta_{ij}\delta_{k\ell}]. \qquad (1.31)$$

The above derivation has been for a molecule with a uniaxial polarizability tensor. For a molecule with three differing polarizabilities along its principal axes, the only changes to (1.28) and (1.29) are the replacements

$$\alpha \to 1/3\ (\alpha_1 + \alpha_2 + \alpha_3) \qquad (1.32)$$

$$(\alpha_2 - \alpha_1)^2 \to \tfrac{1}{2}[(\alpha_1 - \alpha_2)^2 + (\alpha_2 - \alpha_3)^2 + (\alpha_3 - \alpha_1)^2]. \qquad (1.33)$$

We have chosen to write the response function for the nonlinear

polarization (1.29) in an accepted notation. It has been shown[14,18] that the response functions for an important class of mechanisms leading to optical nonlinearities can be cast in the form (1.29). These include Raman, molecular redistribution, and librational contributions to $\chi^{(3)}$. These mechanisms are all governed by the nuclear motion, with the electron clouds following instantaneously in the Born-Oppenheimer approximation. The nuclear response functions a(t) and b(t) give rise to temporal dispersion characterized by poles at the frequencies of the normal modes of the nuclear motion. The mechanisms described by a(t) and b(t) are all local, the excitation does not propagate in this approximation, subvolumes are spatially independent. As a result, the position $\vec{x}$ does not appear in the response function, and hence wavevector dependence, or spatial dispersion, will be absent in the susceptibility. This is not true for the propagating acoustic phonons, as we will see in Section 1.3.

It is desirable to symmetrize, and tensorially decompose the result of (1.29) to agree with the standard response function-susceptibility formalism elaborated in Section 1.2. Symmetrizing, we obtain for (1.29):

$$P_i^{(3)}(t) = \int_0^\infty d\tau' dt_1 dt_2 dt_3 E_j(t - t_1(E_k(t - t_2)E_\ell(t - t_3)$$

$$\times \left\{ \frac{a(\tau')}{3} \cdot \begin{bmatrix} \delta(t_1)\delta(\tau' - t_2)\delta(\tau' - t_3)\delta_{ij}\delta_{k\ell} \\ + \delta(t_2)\delta(\tau' - t_3)\delta(\tau' - t_1)\delta_{ik}\delta_{j\ell} \\ + \delta(t_3)\delta(\tau' - t_1)\delta(\tau' - t_2)\delta_{i\ell}\delta_{jk} \end{bmatrix} \right.$$

cont'd

$$+ \frac{b(\tau')}{6} \cdot \left[\begin{array}{l} \delta(\tau' - t_1)[\delta(\tau' - t_2)\delta(t_3) + \delta(\tau' - t_3)\delta(t_2)]\delta_{ij}\delta_{k\ell} \\ + \delta(\tau' - t_2)[\delta(\tau' - t_3)\delta(t_1) + \delta(\tau' - t_1)\delta(t_3)]\delta_{ik}\delta_{j\ell} \\ + \delta(\tau' - t_3)[\delta(\tau' - t_1)\delta(t_2) + \delta(\tau' - t_2)\delta(t_1)]\delta_{i\ell}\delta_{jk} \end{array} \right] \Bigg\} . \tag{1.34}$$

Carrying out the τ' integration, we identify the time-domain response function:

$$\begin{aligned} \chi^{(3)}_{ijk\ell}(t_1,t_2,t_3) = \delta_{ij}\delta_{k\ell}\Big\{ & \frac{1}{3}\,\delta(t_1)\delta(t_2 - t_3)a(t_2) \\ & + \frac{1}{6}\,b(t_1)[\delta(t_1 - t_2)\delta(t_3) + \delta(t_1 - t_3)\delta(t_2)]\Big\} \\ & + \delta_{ik}\delta_{j\ell}\Big\{\delta(t_2)\delta(t_3 - t_1)a(t_3) \\ & + \frac{1}{6}\,b(t_2)[\delta(t_2 - t_1)\delta(t_3) + \delta(t_2 - t_3)\delta(t_1)]\Big\} \\ & + \delta_{i\ell}\delta_{jk}\Big\{\frac{1}{3}\,\delta(t_3)\delta(t_1 - t_2)a(t_1) \\ & + \frac{1}{6}\,b(t_3)[\delta(t_3 - t_1)\delta(t_2) + \delta(t_3 - t_2)\delta(t_1)]\Big\} . \end{aligned} \tag{1.35}$$

Fourier analyzing, and dividing by four, we obtain the principal result of this section, the nonlinear susceptibility due to field induced molecular reorientation.

$$\chi_{1122}(\omega = \omega_1 + \omega_2 + \omega_3) = \frac{1}{24}\,[2a(\omega_2 + \omega_3) + b(\omega_1 + \omega_2) + b(\omega_1 + \omega_3)] \tag{1.36a}$$

$$\chi_{1221}(\omega = \omega_1 + \omega_2 + \omega_3) = \frac{1}{24}\,[2a(\omega_1 + \omega_2) + b(\omega_1 + \omega_3) + b(\omega_2 + \omega_3)] \tag{1.36b}$$

$$\chi_{1212}(\omega = \omega_1 + \omega_2 + \omega_3) = \frac{1}{24}\,[2a(\omega_1 + \omega_3) + b(\omega_1 + \omega_2) + b(\omega_2 + \omega_3)] \tag{1.36c}$$

where

$$b(\omega) = -\,3a(\omega) = \frac{N(\alpha_2 - \alpha_1)^2}{15kT}\,\frac{1}{1 - i\omega\tau}\,. \tag{1.37}$$

The values of the constants appearing in the susceptibility will be estimated in section 1.5. Here we wish to discuss the resonant behavior exhibited by the reorientational susceptibility.

We are interested in cases where the signals are proportional to $|\chi^{(3)}(\omega = \omega + \Omega - \Omega)|^2$ with ω close to Ω. Evaluating (1.37) we obtain

$$\chi_{1122}(\omega = \omega + \Omega - \Omega) = \frac{1}{24}\left[-\,\frac{2}{3}\,b(0) + \frac{b(0)}{1 + i\Delta\tau}\right] \tag{1.38a}$$

$$\chi_{1221}(\omega = \omega + \Omega - \Omega) = \frac{1}{24}\left[b(0) + \frac{b(0)}{1 + i\Delta\tau}\right] \tag{1.38b}$$

$$\chi_{1212}(\omega = \omega + \Omega - \Omega) = \frac{1}{24}\left[b(0) - \frac{2}{3}\,\frac{b(0)}{1 + i\Delta\tau}\right] \tag{1.38c}$$

where $\Delta = \Omega - \omega$. Eq. (1.38) shows that $\chi^{(3)}(\omega = \omega + \Omega - \Omega)$ has two types of terms. The first type occurs when the argument in a or b in (1.36) corresponds to $\Omega - \Omega = 0$, and gives rise to the nondispersive real contributions proportional to b(0) in Eq. (1.38). These are the terms dictating the ordinary, nonresonant optical Kerr effect. The second type of term has $-\,\Delta = \omega - \Omega$ for the argument of a or b in (1.36). They show resonance when $|\Omega - \omega|\tau \approx 1$. Eq. (1.38) then predicts that a signal proportional to $|\chi^{(3)}(\omega = \omega + \Omega - \Omega)|^2$ will exhibit the interference of the resonant part with half width $\Delta\nu = 1/2\pi\tau$ with the nonreson-

ant background due to the ordinary Kerr effect and possibly other contributing effects. The novelty of our work was the investigation of this resonance using tunable lasers. Also, as we will later show, by proper choice of polarizations, we can "project out" the orientational resonance part of the $\chi^{(3)}$ tensor, thus isolating it from the background optical Kerr and electronic contributions to the susceptibility.

In the development above, it has been tacitly assumed that the electric fields are the local electric fields acting on the molecule. In fact, a local field correction factor

$$L = \frac{\varepsilon(\omega) + 2}{3} \cdot \frac{\varepsilon(\omega_1) + 2}{3} \cdot \frac{\varepsilon(\omega_2) + 2}{3} \cdot \frac{\varepsilon(\omega_3) + 2}{3} \tag{1.39}$$

should multiply the right hand side of (1.36) so that the polarization is correctly related to the macroscopic electric fields.[1,14] However, we shall simply treat the constants a(0) and b(0) in (1.36) as experimental parameters to be determined.

1.4 THE NONLINEAR SUSCEPTIBILITY DUE TO ACOUSTIC PHONON EXCITATION[8-10]

In the absence of absorption and heating, density waves are driven by the electrostrictive pressure

$$P_e = \rho \frac{\partial \varepsilon}{\partial \rho} E^2. \tag{1.40}$$

This pressure arises because the increase in the dielectric constant of a polarizable material, due to compression, will lower the free energy in the presence of a field E.[8,19] Using the Navier-Stokes and continuity equations of hydrodynamics, it is straightforward to derive the

equation for the driven acoustic wave,[8-10] here expressed as a small deviation ρ from the mean fluid density ρ_o:

$$\left[-\nabla^2 + \frac{1}{v^2}\frac{\partial^2}{\partial t^2} + \frac{2\Gamma}{v^2}\frac{\partial}{\partial t}\right]\rho(\vec{r},t) = -\frac{\gamma}{8\pi v^2}\nabla^2 E^2. \tag{1.41}$$

Here γ is the electrostrictive constant $\rho\,\frac{\partial\varepsilon}{\partial\rho}$ which is found to be

$$\gamma = \frac{(\varepsilon - 1)(\varepsilon + 2)}{3} \tag{1.42}$$

from the Clausius-Mossoti relation. v is the velocity of the hypersonic waves; it will become clear that the waves under discussion are of extremely short wavelength $\sim \lambda_{light}$. Γ is the phenomenological damping constant for the acoustic wave. Fourier analyzing the sound wave

$$\rho(\vec{r},t) = \int d^3q\,d\omega_s\,\rho(\vec{q},\omega_s)\exp\, i(\vec{q}\cdot\vec{r} - \omega_s t) \tag{1.43}$$

and making similar analyses of the electric fields via (1.38) we may solve (1.41):

$$\rho(\vec{q},\omega_s) = \frac{\gamma}{8\pi v^2}\,\frac{q^2}{q^2 - \frac{\omega_s^2}{v^2} - \frac{2i\Gamma\omega_s}{v^2}}\int d^3k_1\,d\omega_1\,E(\vec{k}_1,\omega_1)\cdot E(\vec{q}-\vec{k}_1,\omega_s-\omega_1). \tag{1.44}$$

Associated with this field dependent density wave is a change in the dielectric constant, yielding the nonlinear polarization

$$P_i(\vec{r},t) = \frac{1}{4\pi}\Delta\varepsilon(\vec{r},t)E_i(\vec{r},t) = \frac{\gamma}{4\pi\rho_o}\Delta\rho(\vec{r},t)E_i(\vec{r},t). \tag{1.45}$$

Fourier analyzing (1.45) and substituting the result (1.44) for the

density Fourier component, we obtain the result

$$P_i^{(3)}(\vec{k}_4 = \vec{k}_1 + \vec{k}_2 + \vec{k}_3, \omega_4 = \omega_1 + \omega_2 + \omega_3) = \frac{\gamma^2}{32\pi^2\rho_o v^2}$$

$$\times \frac{|\vec{k}_1 + \vec{k}_3|^2}{|\vec{k}_1 + \vec{k}_3|^2 - \frac{(\omega_1 + \omega_3)^2}{v^2} - \frac{2i\Gamma(\omega_1 + \omega_3)}{v^2}} E_i(\vec{k}_2, \omega_2)\vec{E}(\vec{k}_1, \omega_1) \cdot \vec{E}(\vec{k}_2, \omega_2). \tag{1.46}$$

Symmetrizing the result, dividing by four, and making the usual tensor decomposition, we obtain the acoustic phonon contribution to $\overleftrightarrow{\chi}^{(3)}(\vec{k}_4 = \vec{k}_1 + \vec{k}_2 + \vec{k}_3; \omega_4 = \omega_1 + \omega_2 + \omega_3)$:

$$\chi_{1221} = \frac{\gamma^2}{384\pi^2\rho_o v^2} \frac{|\vec{k}_1 + \vec{k}_2|^2}{|\vec{k}_1 + \vec{k}_2|^2 - \frac{(\omega_1 + \omega_2)^2}{v^2} - \frac{2i\Gamma(\omega_1 + \omega_2)}{v^2}} \tag{1.47a}$$

$$\chi_{1122} = \frac{\gamma^2}{384\pi^2\rho_o v^2} \frac{|\vec{k}_2 + \vec{k}_3|^2}{|\vec{k}_2 + \vec{k}_3|^2 - \frac{(\omega_2 + \omega_3)^2}{v^2} - \frac{2i\Gamma(\omega_2 + \omega_3)}{v^2}} \tag{1.47b}$$

$$\chi_{1212} = \frac{\gamma^2}{384\pi^2\rho_o v^2} \frac{|\vec{k}_1 + \vec{k}_3|^2}{|\vec{k}_1 + \vec{k}_3|^2 - \frac{(\omega_1 + \omega_3)^2}{v^2} - \frac{2i\Gamma(\omega_1 + \omega_3)}{v^2}}. \tag{1.47c}$$

Note that the dispersion of the individual tensor elements depends only on fields of like polarization; this is traceable to (1.41) which has the density wave driven by the square of the electric field. Once the acoustic phonon is resonantly excited by the beat note of two of the optical waves present, the third wave involved in the mixing interaction acts as a probe, and determines the polarization direction of $\vec{P}^{(3)}$.

The resonance condition for the Brillouin susceptibility is

$$v^2|\vec{k}_1 + \vec{k}_2|^2 = (\omega_1 + \omega_2)^2. \tag{1.48}$$

Since the sound velocity v is 10^{-5} to 10^{-6} of the light velocity c, and $|\vec{k}_1 + \vec{k}_2|$ is of order k_{light}, only the beat note of two light waves can excite the hypersonic wave. Then the resonance peaks of the susceptibility must occur for temporal Fourier components of opposite sign, and we rewrite (1.48) as

$$v^2|\vec{k}_1 + \vec{k}_2|^2 = (\omega_1 - \omega_2)^2 \tag{1.49}$$

where ω_1 and ω_2 are now assumed to be positive. $\vec{k}_1$ and $\vec{k}_2$ are unrestricted and we take

$$\vec{k}_i = \frac{n\omega_i}{c}\hat{s}_i \tag{1.50}$$

where $\hat{s}_1$ and $\hat{s}_2$ are the propagation direction of the two beams. Then if $\theta = \cos^{-1}(\hat{s}_1 \cdot \hat{s}_2)$ is the angle between the beams, solution of (1.49) to first order in v/c yields the Brillouin resonances

$$\omega_1 - \omega_2 = \pm\,\omega_B = \pm\,\frac{2nv}{c}\,\omega_2 \sin(\theta/2). \tag{1.51}$$

We note that the Brillouin frequency is maximized by choosing $\theta = 180°$ (antiparallel beams) and increases linearly with optical frequency.

1.5 ELECTRONIC CONTRIBUTION TO $\chi^{(3)}$

For a transparent liquid, the electronic contribution to the nonlinear susceptibility is due to the nonresonant excitation of electronic transitions. The weak dispersion and instantaneous response characteristic of these virtual transitions is usually modelled by introducing

a single coupling constant σ:

$$\vec{P}^{(3)}(t) = \sigma\vec{E}(t)\vec{E}(t) \cdot \vec{E}(t). \tag{1.52}$$

This leads to the susceptibility

$$\chi^{(3)}_{ijk\ell} = \frac{\sigma}{24}\,[\delta_{ij}\delta_{k\ell} + \delta_{ik}\delta_{j\ell} + \delta_{i\ell}\delta_{jk}]. \tag{1.53}$$

The equality of χ_{1122}, χ_{1212}, and χ_{1221} implied by this model is called Kleinman's symmetry,[20] and has been tested for a few nonabsorbing samples. Levenson and Bloembergen observed Kleinman symmetry to be accurate to about 20% in benzene;[21] Lynch, Levenson, and Bloembergen also verified the symmetry to about 20% in some cubic fluorides.[22]

1.6 THE NONLINEAR SUSCEPTIBILITY OF CS_2 LIQUID

We chose liquid CS_2 as the sample in our investigation. It has both a large Kerr constant and an intense, narrow, Brillouin doublet, and was thus a good candidate for investigation by a largely unproven spectroscopic technique.

There are two potentially accurate ways of obtaining the value of the parameters in the orientational contribution to $\chi^{(3)}$. The first is to extrapolate the value of $\chi^{(3)}(\omega = \omega + \Omega - \Omega)$ from measurements of the DC Kerr constant of the liquid. The second is to obtain the strength of the orientational contribution by its effect on the coherent Raman lineshape when the Raman strength is known.

The DC Kerr constant is defined as

$$B_o = \frac{\delta n_{\parallel} - \delta n_{\perp}}{\lambda_o E_o^2} \tag{1.54}$$

where $\delta n_{\parallel}$ and $\delta n_{\perp}$ are the DC-field-induced changes in the index of refraction parallel and perpendicular to $\vec{E}_o$. One may derive, from the susceptibility formalism and the wave equation that

$$B_o = \frac{12\omega}{\varepsilon^{\frac{1}{2}}(\omega)c}\left[\chi^{(3)}_{1111}(\omega = \omega + 0 - 0) - \chi^{(3)}_{1122}(\omega = \omega + 0 - 0)\right]. \tag{1.55}$$

Adding the orientational and electronic contributions (1.36) and (1.53) we find

$$B_o = \frac{\omega}{\varepsilon^{\frac{1}{2}}(\omega)c}\,[\sigma + b(0)]. \tag{1.56}$$

One must still correct the values of σ and $b(0)$, obtained by (1.56), for the fact that the Kerr field is an optical field of frequency Ω rather than a DC field. The corrections involve:[14,24] (1) A dispersive correction to the probe wavelength from that used in the DC Kerr measurement. (2) Two Lorentz local field factors (cf. Eq. (1.39)) for the pump frequency. (3) A dispersive correction of $b(0)$ for the pump frequency proportional to the linear polarizability. (4) A dispersive correction to σ.

Using the DC Kerr measurements of Volkova,[25] Owyoung recommends a value $\sigma + b(0) = 5.44 \times 10^{-12}$ esu for $\lambda_\omega = 570$ nm and $\lambda_\Omega = 532$ nm. Using an interferometric measurement of the ratio $\sigma/[\sigma + b(0)]$, he then arrives at the values $\sigma = .69 \times 10^{-12}$ esu and $b(0) = 4.75 \times 10^{-12}$ esu.[24]

By coherent Raman methods, Levenson and Song have calibrated σ and $b(0)$ against separately measured Raman cross sections.[26] They recommend

$\sigma = .48 \times 10^{-12}$ esu and $b(0) = 5.14 \times 10^{-12}$ esu. The wavelengths were $\lambda_\omega = 580$ nm, and $\lambda_\Omega = 550$ nm.

The Brillouin contribution to $\chi^{(3)}$ may be estimated from spontaneous scattering measurements. Kato and Zdasiuk have measured the total Brillouin scattering efficiency S_B at 488 nm.[27] They obtained the value $S_B = 17.9 \times 10^{-6}$/cm/sr. The function

$$I(\omega) = S_B \frac{4\Gamma\left(\omega_B^2 + \Gamma^2\right)}{\left(\omega^2 - \omega_B^2 + \Gamma^2\right)^2 + 4\omega_B^2\Gamma^2} \tag{1.57}$$

was used to fit the experimental lineshape. The Brillouin cross section per wavenumber per steradian is

$$\frac{d^2\sigma}{d\Omega d\bar{\nu}} \equiv \sigma(\bar{\nu}) = \frac{c}{N} I(\omega). \tag{1.58}$$

For $\omega_B \gg \Gamma$, the relationship between the peak Brillouin cross section and the total scattering efficiency is thus

$$\sigma(\bar{\nu})\Big|_{peak} = \frac{c}{N}\frac{S_B}{\Gamma}. \tag{1.59}$$

Owyoung has shown[14] that the relationship between spontaneous cross section and nonlinear susceptibility is

$$\mathrm{Im}[\chi_{1111}(\omega = \omega + \Omega - \Omega)] = -\frac{N\lambda^4}{768\pi^4\hbar c} \times \left[1 - \exp\left(-\frac{\hbar\Delta}{kT}\right)\right]\frac{d^2\sigma}{d\Omega d\bar{\nu}}. \tag{1.60}$$

Here, $\Delta = \Omega - \omega$. It may also be shown[28] that the Brillouin scattering

efficiency is given by

$$S_B = \left(\frac{\omega}{c}\right)^4 \frac{1}{(4\pi)^2} \frac{\gamma^2}{\rho v^2} kT. \tag{1.61}$$

Equations (1.59), (1.60), and (1.61) predict a peak Brillouin nonlinear suceptibility

$$|(\chi_{1111})_{peak}| = \frac{\gamma^2}{768\pi^2 \rho v^2} \frac{\omega_B}{\Gamma} . \tag{1.62}$$

The reader may now verify, by evaluating Eq. (1.47c) at $\chi^{(3)}(\vec{k} = \vec{k} + \vec{K} - \vec{K}; \omega = \omega + \Omega - \Omega)$ for the Brillouin resonance $|\vec{k} - \vec{K}|^2 = \omega_B^2/v^2$, and taking $\chi_{1111} = \chi_{1212}$, that Eqs. (1.47), (1.60), and (1.61) are all consistent. Thus our susceptibility calculation agrees with the Brillouin scattering efficiency formula using Owyoung's relationship between cross section and susceptibility.

Using (1.59), (1.60), and (1.61) we may derive the relationship between peak susceptibility and scattering efficiency. We obtain

$$|\chi_{1111}|_{peak} = \frac{1}{48} \frac{1}{(\omega/c)^4} \frac{\omega_B}{kT} \frac{S_B}{\Gamma} . \tag{1.63}$$

This shows that the ω^4 dependence of the scattering efficiency cancels out of the susceptibility value; as Eq. (1.62) shows $\chi_{1111} \propto \omega_B$. Thus we may estimate $\chi^{(3)}_{peak}$ using $(\omega/c)^4$ and S_B at 488 nm from ref. 27, but using ω_B at our wavelength, 590 nm. Using the hypersonic velocity[27] $v = 1.26 \times 10^5$ cm/sec, $S_B = 17.9 \times 10^{-6}$ cm^{-1} sr^{-1}, a linewidth (FWHM) $\Gamma/\pi =$ 71 MHz obtained from an average of stimulated scattering measurements,[10] we obtain $\omega_B = 6.9$ GHz and $\chi^{(3)}_{peak} = 6.5 \times 10^{-12}$ esu.

This is about 5 times as large as that for the 656 cm^{-1} Raman mode in CS_2, and suggests that coherent Brillouin signals should be easily observable with equipment similar to that of workers in coherent Raman spectroscopy. We next review the experimental techniques of coherent Raman spectroscopy.

Figure Caption

Fig. 1.1 Polar representation of the orientation of an axisymmetric molecule.

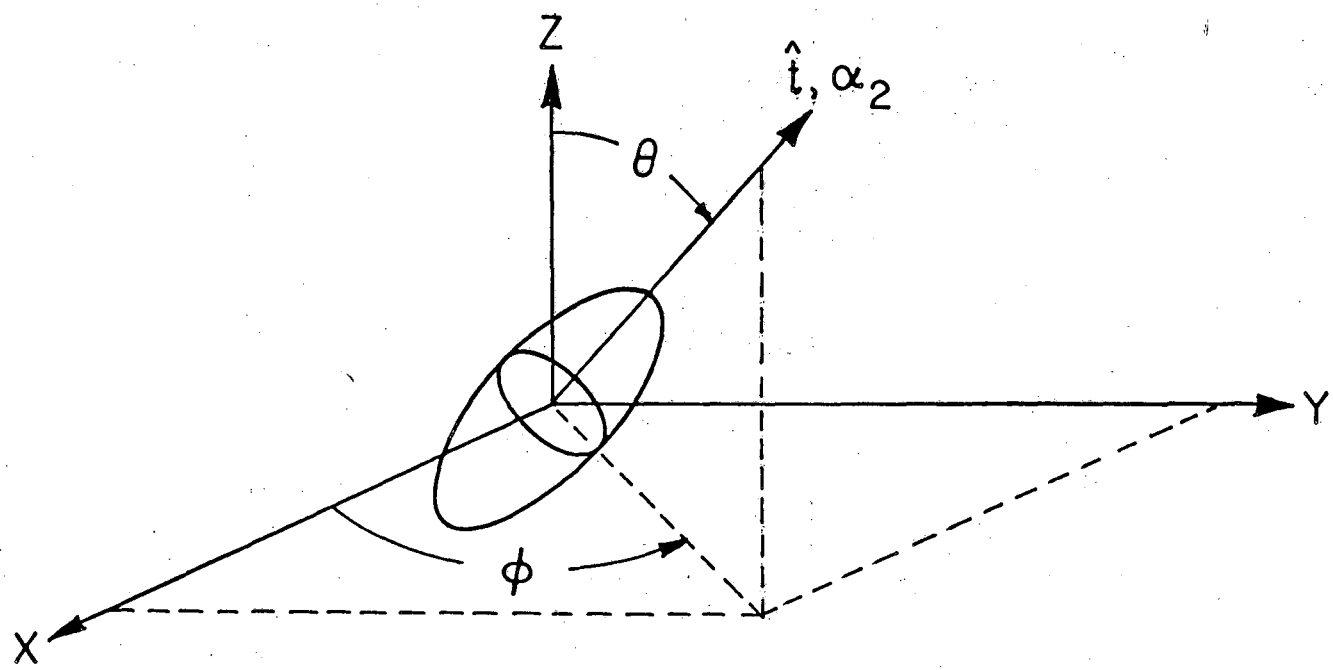

XBL 823-5336

Figure 1.1

2. COHERENT RAMAN SPECTROSCOPY

2.1 INTRODUCTION

In Chap. 1 we showed, via the calculation of nonlinear susceptibilities, how a third-order nonlinear polarization can arise due to the molecular reorientation or acoustic phonon mechanisms. Here, we discuss the nonlinear spectroscopy of these excitations. The general class of experimental techniques used, coherent Raman spectroscopy, was first applied to the study of molecular vibrations. Our work is thus a natural extension of these techniques towards the spectral region of near zero Raman shift.

In coherent Raman spectroscopy,[29-31] the nonlinear polarization acts as a radiation source to generate a coherent beam of light containing the spectral information. The coherent nature of the signal gives the technique its advantages. First, the small angular divergence of the signal permits discrimination from background light by spatial filtering. Thus, it is possible to study fluorescing samples,[32] or to do investigations in flames,[33] discharges,[34] jet engines,[35] etc. where there is much collateral thermal radiation. Second, coherent Raman techniques have intrinsically high resolution due to the nature of the laser sources employed. In spontaneous scattering, a monochromatic beam is scattered simultaneously into all possible channels, and the resolution will be characteristic of the spectrometer used to disperse the light. Invariably, one must trade off signal level in order to obtain higher resolution. In coherent Raman spectroscopy, two laser sources coherently drive the material excitation at their difference frequency. Only scattering channels within this bandwidth are excited, and the signal beam

can be many orders of magnitude more powerful than spontaneously scattered light.[29] A third advantage is the additional control over experimental variables afforded by two or more beams used in the excitation. The output signal may be purposely generated at a frequency of small absorption or fluorescence, the polarization of the beams may be used for additional signal discrimination or to separate the effects of different material excitations, and control of the beam directions permits study of excitations with spatial dispersion, or permits spatially resolved spectroscopy by creating a spatially localized nonlinear polarization.

The nonlinear optical processes to be discussed we divide into two classes. In the first, four wave mixing, two or three input beams interact to generate a signal beam of distinct frequency and wavevector. The amplitude and polarization-sensitive CARS techniques are discussed as examples. The second class of techniques are derived from stimulated Raman scattering. Here, a pump beam induces a gain or loss and phase shift on the components of the probe beam. When a beam of new polarization is created, we have the optical Kerr effect, or RIKES scheme used in our experiment. When only gain or loss are detected, we have Raman gain or loss spectroscopy. The intermediate situation, in which the nonlinear signal is permitted to coherently admix with the input probe beam acting as local oscillator, is called OHD-RIKES or optically-heterodyned polarization interferometry. In the plane wave approximation, we derive a single expression that covers all the stimulated Raman techniques, for arbitrary pump polarization. This will be used in Chap. 4 to analyze the data.

2.2 FOUR WAVE MIXING

In all nonlinear spectroscopic techniques, the nonlinear polarization acts as a source term in the forced wave equation

$$\left[\nabla^2 - \frac{\varepsilon}{c^2}\frac{\partial^2}{\partial t^2}\right]\vec{E}(\vec{r},t) = \frac{4\pi}{c^2}\frac{\partial^2}{\partial t^2}\vec{P}^{NL}(\vec{r},t). \tag{2.1}$$

In four wave mixing, three input beams interact to generate a nonlinear polarization of distinct frequency and wavevector. In the plane wave approximation, we may write the nonlinear polarization as

$$P_i^{NL}(\vec{r},t) = D\chi_{ijk\ell}(\omega = \omega_1 + \omega_2 - \omega_3)E_j(\omega_1)E_k(\omega_2)E_\ell^*(\omega_3)$$

$$\times \exp i[(\vec{k}_1 + \vec{k}_2 - \vec{k}_3)\cdot\vec{r} - \omega t]. \tag{2.2}$$

The solution of (2.1) and (2.2) in the slowly growing wave, and steady state approximations is

$$\vec{E}(\vec{r},t) = \vec{\mathcal{E}}(z)e^{i(kz-\omega t)} \tag{2.3}$$

where

$$\mathcal{E}_i(z) = \frac{i2\pi\omega z}{\varepsilon^{\frac{1}{2}}c} D\chi_{ijk\ell}E_j(\omega_1)E_k(\omega_2)E_\ell^*(\omega_3)\left[\frac{\exp(i\Delta k_z z) - 1}{\Delta k_z z}\right]. \tag{2.4}$$

where

$$\Delta\vec{k} = \vec{k}_1 + \vec{k}_2 + \vec{k}_3 - k\hat{z} \tag{2.5}$$

and we have assumed zero input field and have ignored an unimportant transverse phase factor. Equation (2.4) shows that the signal intensity will vary as

$$I(\omega) \propto z^2 |\chi^{(3)} : \hat{e}_1 \hat{e}_2 \hat{e}_3^*|^2 I(\omega_1) I(\omega_2) I(\omega_3) \tag{2.6}$$

provided that the phase mismatch $\Delta\vec{k} \cdot \hat{z}$ is zero. If it is not, (2.6) must be reduced by the factor $\sin^2(\frac{1}{2}\Delta\vec{k} \cdot \vec{z})/(\frac{1}{2}\Delta\vec{k} \cdot \vec{z})^2$. In Eq. (2.6) $\hat{e}_i$ are the complex polarization vectors of the input fields.

The most important advantage of the four wave mixing scheme just presented is that a wave of new frequency ω is generated. Using interference filters, prisms, or monochromators, even very weak 4 WM signals may be detected above the stray light of the pump beams. The phase matching condition can be satisfied in a variety of ways.[36-38] In one technique, called BOXCARS,[36] the beams are intentionally made to cross at large angles to define a small interrogated volume for spatial resolution.

The principal disadvantage of 4WM is the signal's dependence on the square of the susceptibility. This causes all contributions of the nonlinear susceptibility to interfere constructively and destructively, possibly distorting or masking the Raman resonance at ω_2 (or ω_1) $- \omega_3 = \omega_R$. Sometimes this is not bad. In a pure substance, if the parameters governing the Raman resonance are known accurately, the 4WM dispersion can be used to deduce the values of the electronic and orientational contributions to $\chi^{(3)}$ by curve fitting.[23,26] This is one of the best ways to obtain such data. However, in analytical applications, one might want to detect a trace substance by the signature of its Raman reson-

ance. Since the desired signal is proportional to the square of the concentration, the sensitivity will be poor for high dilution. Moreover, the background contribution of the diluent may be much larger than the resonant contribution of the trace molecules. Due to the typical 5-20% rms fluctuations of the pulsed laser usually employed, fluctuations of the background-dominated 4WM signals will swamp the Raman resonance. A solution to this problem likes in making use of the different spatial dependences of the background and resonant contributions to the $\chi^{(3)}$ tensor. We close our discussion of 4WM spectroscopy by illustrating the technique of polarization-sensitive CARS as one means of background suppression.[39-41] (For other examples of background cancellation schemes, see ref. 41. For a critical analysis of analytical capability, see ref. 31.)

In CARS, two of the pump waves are provided by a single beam, and the nonlinear polarization is given by

$$P_i(\omega_B) = 3\chi_{ijk\ell}(\omega_3 = \omega_1 + \omega_1 - \omega_2)E_j(\omega_1)E_k(\omega_1)E_\ell^*(\omega_2). \qquad (2.7)$$

Let the complex polarization vectors of the ω_1 and ω_2 beams be $\hat{e}_1$ and $\hat{e}_2$. The tensor and permutation symmetries of $\overleftrightarrow{\chi}^{(3)}$ imply that the radiated field in CARS will be proportional to the vector

$$\vec{A} = \vec{A}^R + \vec{A}^{NR} = \chi_{1221}(\hat{e}_1 \cdot \hat{e}_1)\hat{e}_2^* + 2\chi_{1122}(\hat{e}_1 \quad \hat{e}_2^*)\hat{e}_1 \qquad (2.8)$$

$$\vec{A}^R = \chi^R_{1221}(\hat{e}_1 \cdot \hat{e}_1)\hat{e}_2^* + 2\chi^R_{1122}(\hat{e}_1 \cdot \hat{e}_2^*)\hat{e}_1 \qquad (2.9a)$$

$$\vec{A}^{NR} = \chi^{NR}_{1221}(\hat{e}_1 \cdot \hat{e}_1)\hat{e}_2^* + 2\chi^{NR}_{1122}(\hat{e}_1 \cdot \hat{e}_2^*)\hat{e}_1. \qquad (2.9b)$$

In Eq. (2.8), we have separated the CARS source vector $\vec{A}$ into the resonant and nonresonant contributions (2.9). These fields are in general not parallel, and the background contribution (2.9b) may be rejected by a suitable analyzer. Let us consider a simple, but realistic example. Define a depolarization ratio ρ:

$$\rho = \chi_{1221}/\chi_{1111}. \tag{2.10}$$

Let us consider a perfectly polarized Raman contribution having $\rho = 0$ being interfered with by a background electronic contribution exhibiting Kleinman's symmetry, Eq. (1.55). For this contribution, $\rho = 1/3$. Then Eq. (2.9) may be written

$$\vec{A}_R = \chi^R_{1111}(\hat{e}_1 \cdot \hat{e}_2^*)\hat{e}_1 \tag{2.11a}$$

$$\vec{A}_{NR} = \frac{1}{3}\chi^{NR}_{1111}[(\hat{e}_1 \cdot \hat{e}_1)\hat{e}_2^* + 2(\hat{e}_1 \cdot \hat{e}_2^*)\hat{e}_1]. \tag{2.11b}$$

Then an analyzer, $\hat{p}$, satisfying

$$(\hat{e}_1 \cdot \hat{e}_1)(\hat{e}_2^* \cdot \hat{p}) + 2(\hat{e}_1 \cdot \hat{e}_2^*)(\hat{e}_1 \cdot \hat{p}) = 0 \tag{2.12}$$

will transmit the CARS signal radiated by

$$(\hat{p} \cdot \vec{A}_R)\hat{p} = -\tfrac{1}{2}\hat{p}\chi^R_{1111}(\hat{e}_1 \cdot \hat{e}_1)(\hat{e}_2^* \cdot \hat{p}) \tag{2.13}$$

with the nonresonant contribution entirely eliminated. It can be shown that for linearly polarized pump beams, the orientation of $\hat{e}_1$, $\hat{e}_2$, and $\hat{p}$

which simultaneously eliminates the background and maximizes the CARS signal is: $\hat{e}_1$ and $\hat{p}$ make 120° angle, $\hat{e}_2$ lies on the bisector of this angle. In this case, the Raman signal is reduced by a factor of 16 from the case of parallel pump beams, but the background may be rejected by factors approaching 10^4 (ref. 40).

The use of polarization techniques in CARS make this type of 4WM scheme more powerful. For instance, the polarization state of the vector $\vec{A}$ in Eq. (2.8) may be analyzed directly as a function of frequency, yielding the technique of "Coherent Raman Elipsometry" (CREM).[39] In this way, it has proven possible to detect Raman lines separated in frequency by distances smaller than the homogeneous line widths.[39,41] In a related application, polarizations may be arranged such that a small admixture of the background signal may be used to cancel a strong resonant signal, thereby revealing a weaker resonance in its wings.[40] This is a kind of "optical heterodyne CARS" where the nonresonant background provides the local oscillator. A full treatment of CARS variants, and comparison with the stimulated Raman techniques discussed below, appears in ref. 31.

2.3 STIMULATED RAMAN SPECTROSCOPY

In stimulated Raman spectroscopy (SRS) a pump beam at frequency Ω induces a gain, loss, or phase shift on a probe beam at ω. In contrast to the four wave mixing schemes described above, the reaction of the field generated by the nonlinear mixing on one of the input fields is intrinsic to the process, and cannot be neglected. Moreover, SRS processes are automatically phase matched. These properties bring a new set of advantages to nonlinear spectroscopy which will emerge in the

discussion below.

The SRS nonlinear polarization, neglecting wavevector dependence, is given by

$$P_i^{(3)}(\omega) = 6\chi_{ijk\ell}(\omega = \omega + \Omega - \Omega)E_j(\omega)E_k(\Omega)E_\ell^*(\Omega). \tag{2.14}$$

For the general elliptically polarized pump beam, following Fig. 2.1, we may write

$$\vec{E}(\Omega) = (a\hat{\xi} + ib\hat{\eta})\mathcal{E}(\Omega)$$

$$= [\hat{x}(a\cos\psi - ib\sin\psi) + \hat{y}(a\sin\psi + ib\cos\psi)]\mathcal{E}(\Omega) \tag{2.15}$$

where a and b are real, and $a^2 + b^2 = 1$. Making the slow wave approximation, and ignoring pump beam depletion, the SRS process is governed by the coupled equations:

$$\frac{\partial\mathcal{E}_x(\omega)}{\partial z} = i\gamma[(\chi_A + g\chi_B)\mathcal{E}_x(\omega) + (h\chi_B - if\chi_c)\mathcal{E}_y(\omega)]$$

$$\frac{\partial\mathcal{E}_y(\omega)}{\partial z} = i\gamma[(h\chi_B + if\chi_c)\mathcal{E}_x(\omega) + (\chi_A - g\chi_B)\mathcal{E}_y(\omega)] \tag{2.16}$$

where

$$\gamma = (6\pi\omega/\varepsilon^{\frac{1}{2}}c)|\mathcal{E}(\Omega)|^2 \tag{2.17}$$

$$\chi_A = \chi_{1111} + \chi_{1122} \tag{2.18a}$$

$$\chi_B = \chi_{1111} - \chi_{1122} \tag{2.18b}$$

$$\chi_c = \chi_{1212} - \chi_{1221} \tag{2.18c}$$

$$f = 2ab \tag{2.19a}$$

$$g = (a^2 - b^2)\cos 2\psi \tag{2.19b}$$

$$h = (a^2 - b^2)\sin 2\psi. \tag{2.19c}$$

For arbitrary $\vec{\mathcal{E}}_o(\omega)$ at $z = 0$, the solution for Eq. (2.16) is

$$\begin{pmatrix} \mathcal{E}_x(\omega) \\ \mathcal{E}_y(\omega) \end{pmatrix} = \begin{pmatrix} \mathcal{E}_1 \\ \mathcal{E}_2 \end{pmatrix} e^{i\gamma S_+ z} + \begin{pmatrix} \mathcal{E}_3 \\ \mathcal{E}_4 \end{pmatrix} e^{i\gamma S_- z} \tag{2.20}$$

where the eigenvalues S_+ and S_- are given by

$$S_\pm = \chi_A \pm \sqrt{(g^2 + h^2)\chi_B^2 + f^2\chi_c^2} \tag{2.21}$$

and

$$\mathcal{E}_1 = \frac{\mathcal{E}_{xo}(\chi_A + g\chi_B - S_-) + \mathcal{E}_{yo}(h\chi_B - if\chi_c)}{S_+ - S_-} \tag{2.22a}$$

$$\mathcal{E}_2 = \frac{\mathcal{E}_{xo}(h\chi_B + if\chi_c) - \mathcal{E}_{yo}(\chi_A + g\chi_B - S_+)}{S_+ - S_-} \tag{2.22b}$$

$$\mathcal{E}_3 = \frac{-\mathcal{E}_{xo}(\chi_A + g\chi_B - S_+) - \mathcal{E}_{yo}(h\chi_B - if\chi_c)}{S_+ - S_-} \tag{2.22c}$$

$$\mathcal{E}_4 = \frac{-\mathcal{E}_{xo}(h\chi_B + if\chi_c) + \mathcal{E}_{yo}(\chi_A + g\chi_B - S_-)}{S_+ - S_-} . \qquad (2.22d)$$

This solution greatly simplifies if the pump beam is either purely linearly or circularly polarized. Equation (2.16) then becomes diagonalizable with solution

$$\vec{\mathcal{E}}(\omega) = \hat{\alpha}[\exp(g_\alpha/2 + i\delta_\alpha)z]\mathcal{E}_{\alpha o} + \hat{\beta}[\exp(g_\beta/2 + i\delta_\beta)z]\mathcal{E}_{\beta o} \qquad (2.23)$$

where $\hat{\alpha}$ is the complex polarization of the pump beam, $\hat{\beta}$ is the polarization vector orthogonal to the pump, and $g_\alpha(\delta_\alpha)$ and $g_\beta(\delta_\beta)$ are the intensity gain factors per unit length (phase shifts per unit length) for probes parallel, and orthogonal to the pump beam, respectively. $\mathcal{E}_{\alpha o}$ and $\mathcal{E}_{\beta o}$ are the initial amplitudes of the probe beam. We are now in a position to discuss the family of SRS techniques.

A. RAMAN GAIN SPECTROSCOPY

One can first of all measure the amplification or attenuation of the probe due to the pump via the Raman process. For $\Omega > \omega$, we have gain via stimulated Raman scattering. When $\omega < \Omega$ we have loss via the inverse Raman effect.[43] These emerge naturally from the signs of $\mathrm{Im}(\chi^{(3)})$ at resonance.

For the cases in which the stimulated Raman interaction is diagonalizable, $g_{\alpha,\beta}$ and $\delta_{\alpha,\beta}$ of Eq. (2.23) are given by

$$g_{\alpha,\beta} = -\frac{24\pi\omega}{\varepsilon^{\frac{1}{2}}c}|\mathcal{E}(\Omega)|^2\chi_{eff}^{(3)''}(\omega = \omega + \Omega - \Omega) \qquad (2.24a)$$

$$\delta_{\alpha,\beta} = \frac{12\pi\omega}{\varepsilon^{\frac{1}{2}}c}|\ (\Omega)|^2 \chi_{eff}^{(3)'}(\omega = \omega + \Omega - \Omega) \tag{2.24b}$$

where

$$\chi_{eff}^{(3)} = \chi_{eff}^{(3)'} + i\chi_{eff}^{(3)''}$$

$$= \hat{e}_{\omega}^{*} \cdot \overleftrightarrow{\chi}^{(3)} : \hat{e}_{\omega}\hat{e}_{\Omega}\hat{e}_{\Omega}^{*}. \tag{2.25}$$

Table 2.1 lists $\chi_{eff}^{(3)}$ for the diagonalizable cases.

For small gain, Eq. (2.23) implies the gain signal

$$S = P(\omega)[1 + G(\omega - \Omega)] \tag{2.26}$$

where $G(\omega - \Omega)$ is given by the appropriate gain evaluated from (2.24a) times a spatial integral over the pump and probe beam profiles. Note that G is linearly proportional to $\mathrm{Im}(\chi^{(3)})$. Also, from Table 2.1, it is evident that a set of three gain measurements can accurately characterize $\mathrm{Im}(\chi^{(3)})$.

The linear dependence on the susceptibility causes the Raman gain signal to decrease much less strongly with species density and cross section than in four wave mixing. Also, since Raman gain is governed by $\mathrm{Im}(\chi^{(3)})$, the usually real background susceptibilities present do not distort the signal.

The Raman gain signal can be quite strong. For pump and probe beams of identical Gaussian profiles interacting coaxially in a sample cell many confocal parameters long, the gain signal is given by:[44]

Table 2.1

Polarization Configuration	$\chi^{(3)}_{eff}(\omega = \omega + \Omega - \Omega)$
Probe, pump: same linear	χ_{1111}
Probe, pump: opposite linear	χ_{1122}
Probe, pump: same circular	$\chi_{1122} + \chi_{1212}$
Probe, pump: opposite circular	$\chi_{1122} + \chi_{1221}$

$$\frac{\Delta P(\omega)}{P(\omega)} = G(\omega - \Omega) = \frac{384\pi^4}{\lambda^2 cn}\left[- \mathrm{Im}\chi^{(3)}_{eff}\right]P(\Omega) \tag{2.27}$$

where $\lambda^2 = (2\pi c)^2\omega^{-1}\Omega^{-1}$ and $\chi^{(3)}_{eff}$ may be found from Table 2.1. As an example, for benzene $\chi^{(3)} \approx 3 \times 10^{-13}$ esu, and for $P(\omega) = 50$ mW, $\lambda_\omega = 633$ nm, $\lambda_\Omega = 595$ nm, $\Delta P(\omega)/P(\omega) = 3.3 \times 10^{-5}$. This is observable using low noise CW lasers and synchronous detection.[44]

From Raman gain spectroscopy, it is useful to consider the ultimate signal to noise ratio, given by[45,46]

$$\frac{S}{N} = \frac{G}{\left[\delta_\Omega G^2 + \delta_\omega + 2\,\frac{\hbar\omega\Delta\nu}{QP(\omega)}\right]^{\frac{1}{2}}}. \tag{2.28}$$

Here G is the fractional gain induced on the probe beam, and δ_ω and δ_Ω are the mean squared fractional deviation of the pump and probe beam powers within the detection bandwidth $\Delta\nu$. The last term in the denominator is the shot-noise contribution;[47] Q is the quantum efficiency of the detector. For small gain, the pump beam fluctuation noise may be neglected, and when the probe beam fluctuation dominates, Eq. (2.28) reduces to the result that the S/N ratio is one when the induced gain equals the rms probe fluctuation in one integration time. Owyoung has extensively studied the application of Raman gain as a sensitive technique.[44-46,48,49] He concludes that due to probe fluctuations, the shot noise limit is never reached. The advantages of Raman gain are (1) large signal level, especially with pulsed laser pump, (2) direct display of polarized and depolarized spectra, (3) simplicity of set-up allowing signal enhancement by multipass configuration, and (4) elimination of effects of real background contributions to the susceptibility. We would add a fifth advantage of gain measurements, yet to be demonstrated, which is the

possibility of making an absolute Raman cross section measurement.

B. RAMAN INDUCED KERR EFFECT

In the optical Kerr effect, the medium is rendered anisotropic to a probe beam by the presence of a pump beam in Raman resonance to the probe. The anisotropy comes about due to coherent radiation by the nonlinear medium into a polarization state orthogonal to the input probe beam. The signal is detected by monitoring the probe beam through suitable analyzers.

The Raman induced Kerr effect scheme (RIKES) was originally proposed as a background-free coherent Raman method.[50] Suppose the probe beam at ω enters the sample polarized along $\hat{x}$, and $|\mathcal{E}_y(\omega)|^2$ is detected. If the gain is small, then application of Eqs. (2.20 - 2.22) yields the RIKES signal:

$$|\mathcal{E}_y(\omega)|^2 \propto |(a^2 - b^2)\sin 2\psi(\chi_{1212} + \chi_{1221}) + i2ab(\chi_{1212} - \chi_{1221})|^2$$

$$\times P^2(\Omega)P(\omega). \qquad (2.29)$$

For a circularly polarized pump wave, a = b, and the dispersion of the signal is governed by $|\chi_{1212}(\omega = \omega + \Omega - \Omega) - \chi_{1221}(\omega = \omega + \Omega - \Omega)|^2$. Thus background electronic contributions satisfying Kleinman's symmetry cancel, but the Raman mode contributes through $\chi_{1212}(\omega = \omega + \Omega - \Omega)$. This, and the automatic phase matching property, gave RIKES an advantage over the amplitude CARS technique. Another advantage of RIKES is its ability to obtain spectra as $|\omega - \Omega|$ tunes through zero.[16] This is critical in our work. Also, as we will show in Chap. 4, the background

Kerr effect contribution is cancelled for a circularly polarized pump.[16] Thus, we could display the coherent Rayleigh-wing spectrum with high contrast. Finally, the Brillouin contribution is always present in the spectra, having the tensor properties of a completely polarized mode. The above advantages made RIKES a good technique for demonstrating coherent Rayleigh-Brillouin spectroscopy.

As a sensitive technique, RIKES has some serious disadvantages. Like CARS, the signal is proportional to the square of the susceptibility, causing it to be small at low concentrations. The worst problem is the background due to imperfect crossing of polarizer and analyzer. Extinction of better than 10^{-7} is very difficult; we estimate our extinction at $\sim 10^{-6}$. This should be contrasted with the spectral discrimination of 10^{12} - 10^{14} available using double monochromaters in CARS. The solution to these problems is addressed by the OHD-RIKES technique.

In optically-heterodyned RIKES (OHD-RIKES), or polarization interferometry, a small component of the probe beam is permitted to leak through the analyzer and fall on the detector.[46,51-53] There, it acts as a local oscillator, interfering with the nonlinear signal. By controlling the local oscillator amplitude, the resulting signal is made linear in the susceptibility. By controlling its phase, either the real or imaginary parts of the effective susceptibility may be displayed.

Consider again the optical Kerr effect scheme in which the intensity $S = |\mathcal{E}_y(\omega,z)|^2$ is detected. Let the input probe field be given by

$$\vec{\mathcal{E}}_o(\omega,0) = \hat{x}\mathcal{E}_o + \hat{y}\mathcal{E}_o k e^{i\delta}. \tag{2.30}$$

Here k is the relative amplitude of the local oscillator ($k \ll 1$) and δ

is its phase. From Eq. (2.20), the detected signal is given by

$$\mathcal{E}_y(\omega,z) = \mathcal{E}_2 e^{i\gamma S_+ z} + \mathcal{E}_4 e^{i\gamma S_- z}$$

$$\approx \mathcal{E}_2 + \mathcal{E}_4 + i\gamma z(S_+\mathcal{E}_2 + S_-\mathcal{E}_4). \qquad (2.31)$$

Use of Eqs. (2.22) and (2.23), and neglecting terms of order lower than $|k\chi^{(3)}|$, we obtain the OHD-RIKES signal:

$$S = |\mathcal{E}_o|^2\{k^2 + 2k\gamma z \cos\delta[- h\mathrm{Im}(\chi_B) - f\mathrm{Re}(\chi_c)]$$

$$+ 2k\gamma z \sin\delta[h\mathrm{Re}(\chi_B) - f\mathrm{Im}(\chi_c)]\}. \qquad (2.32)$$

Here, h and f are pump polarization ellipse parameters (Eq. (2.19)), $\chi_B = \chi_{1212} + \chi_{1221}$, and $\chi_c = \chi_{1212} - \chi_{1221}$. The cases of linear and circular polarized pumps, and of local oscillator phases of 0 and $\pi/2$ are of interest due to the separation of the real and imaginary parts of the susceptibility. These results are summarized in Table 2.2. Note that for the measurements shown, the OHD-RIKES always displays the difference between the polarized and depolarized spectra.

The advantage of OHD-RIKES is that the noise due to probe fluctuations is rejected by the analyzer by a factor k^2, but the OHD-RIKES signal is proportional to k. Thus the OHD-RIKES scheme is able to overcome the major source of noise in Raman gain, probe fluctuations, by a factor of k. For OHD-RIKES, the ultimate S/N ratio has been calculated:[46]

Table 2.2 OHD-RIKES Configurations

	Local Oscillator Phase	
	$\delta = 0$	$\delta = \pi/2$
linear pump	$\chi''_{1111} - \chi''_{1122}$; linear dichroism	$\chi'_{1111} - \chi'_{1122}$; linear birefringence
circular pump	$\chi'_{1212} - \chi'_{1221}$; circular birefringence	$\chi''_{1212} - \chi''_{1221}$; circular dichroism

$$\frac{S}{N} = \frac{\frac{k}{2}\,G}{\left[k^4\delta_\omega + 2e\left(\frac{\hbar\omega}{eQ}\right)\frac{k^2\Delta\nu}{P(\omega)} + \left(\frac{\hbar\omega}{eQP(\omega)}\right)^2\left(2ei_d\Delta\nu + \frac{4kT}{R}\,\Delta\nu\right)\right]^{\frac{1}{2}}} \,. \qquad (2.33)$$

The noise terms in the denominator, are, in order, probe fluctuation noise, probe shot noise, and detector dark current shot noise, and Johnson noise in the detector load resistance. Note that in the limit that probe fluctuations have been made negligible, the probe shot noise limit of S/N (2.32) is independent of k. Then, the ability to maximize the S/N is dependent on the ability to minimize the dark current and Johnson noise contributions. These may be minimized by suitably large probe power $P(\omega)$. In general, there is an optimal level of local oscillator present for a given experimental situation; this is discussed in ref. 53.

OHD-RIKES is thus able to overcome the probe noise problems of Raman gain. Its principal disadvantages are: (1) The output is proportional to a dichroism or birefringence, and represents the difference between the polarized and depolarized spectra. (2) The more complicated optical set-up does not lend itself well to enhancement of a weak signal by multiple passes through the sample. The first problem is not so important in analytical applications when the polarization properties of the species being detected are well understood. However, in initial investigations of the $\chi^{(3)}$ tensor elements, the OHD-RIKES measurements would have to be backed up by Raman gain measurements to unambiguously characterize the tensor properties of the susceptibility. The problem with multipass set-ups can be overcome by careful optical design, high-quality optical elements, and a separate arm to control the phase and amplitude of the local oscillator, so that it does not have to multipass the sample.[53]

In conclusion, we have described the principal coherent Raman techniques. The control over experimental parameters and signal to noise advantages of these techniques give the coherent Raman field a bright future.

Figure Caption

Fig. 2.1 Parameters of elliptical polarization state.

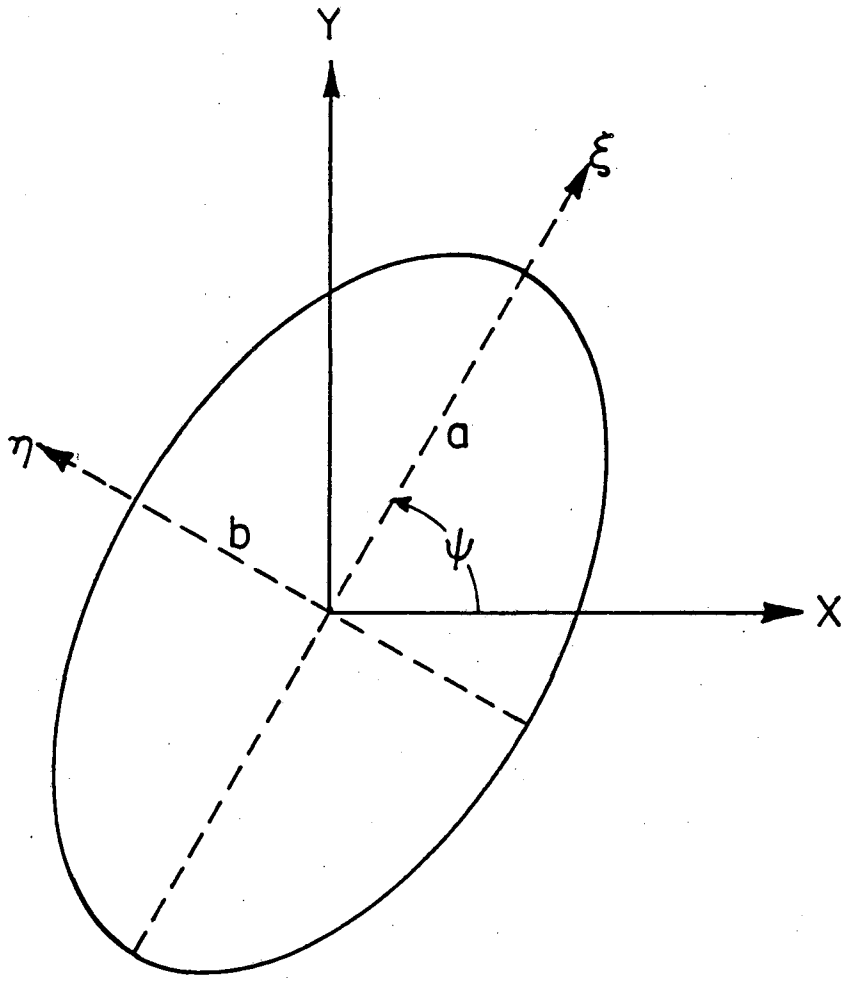

Figure 2.1 XBL 823-5337

3. THE EXPERIMENTAL APPARATUS

We were interested in extending the RIKES scheme to the Brillouin and Rayleigh-wing regime. The experimental set-up involved a pair of nitrogen laser pumped dye lasers. The nitrogen laser, dye lasers, and RIKES spectrometer were all built in our laboratory and in the Department shops.

3.1 THE NITROGEN LASER

The molecular nitrogen laser[54-60] operates at 337 nm and was used as a dye laser pump. The lasing takes place between the excited $C^3\pi$ and $B^3\pi$ states of the molecule in a fast, medium pressure, electric discharge. Inversion is produced when ground $X^1\Sigma$ molecules are excited to the C state, in preference to the B state, due to the larger Franck-Condon overlap factor for the former two states.[56] The short radiative lifetime of the upper state, 40 ns, and the fact that only the > 10 eV tail of the electron Boltzmann distribution is effective in creating the inversion, dictate a fast, high-current discharge. The long lifetime of the lower level, 6 μsec, causes the N_2 laser to self-terminate due to lower level "bottle-necking."

To produce the fast discharge necessary for laser action in N_2 poses a conflict between performance and reliability. It is desirable to operate with as high a voltage as possible. For given energy storage, this lowers the capacitance needed, thus lowering the capacitive discharge time. However, to obtain the necessary insulation to prevent the laser from shorting, one wishes to separate the conductors, thus increasing the inductance and slowing the discharge. The problem reduces to build-

ing a transmission line with lowest possible characteristic impedance operating at as high a voltage as possible with acceptable reliability. Finally, it is very important that the laser be quickly repairable should a high voltage fault occur.

We studied four different N_2 laser designs having the two circuit diagrams shown in Fig. 3.1. The first type of laser used the circuit of Fig. 3.1a in experimental devices shown in Fig. 3.2. Reference to these figures show that the laser tube is in series with one conductor of a parallel plate transmission line formed by capacitors C_1 and C_2. Laser action occurs when the discharge wave of the line reaches the laser tube after switch S closes. The charging resistors R_c and r are open circuits during the fast discharge. This is the "Blumlein" design. Typically, C_1 and C_2 were square, 600 mm on a side, and had 1.6 mm sheet metal conductors separated by three .13 mm thick mylar sheets. The switches were small spark gaps and the units were operated at 15 kV and 10 pps. The cavity was formed by a flat aluminum mirror and an uncoated quartz flat and the beam was rectangular with dimensions 5 × 20 mm. The single sided Blumlein devices gave out pulse energies of .7 to 1.4 mJ; the double-sided lasers attained 1.8 to 2.3 mJ. The FWHM pulselengths were 3 to 5 ns and the operating pressures were 50 to 80 torr.

While the performance was impressive for such primitive devices, it was really not adequate for our experiments. We needed more power, longer pulselengths, and more reliability.

The next N_2 laser built used the "capacitor transfer" circuit of Fig. 3.1b. The energy is initially stored in capacitor C_1 which is charged through resistors r and R_c. When S closes, C_1 is connected across C_2 and the laser tube. C_2 acts as a transmission line or "dump-

ing capacitor" to provide a low inductance path for current flow from C_1 to the laser tube. As before, the charging resistors are out of the circuit on the time scale of the discharge. We built a double-sided capacitor transfer laser according to the design described in ref. 55. A cross section of the laser head is shown in Fig. 3.3; the reader is referred to ref. 55 for further details.

Figure 3.4 shows the operating characteristics of this laser at 10, 20, and 30 Hz repetition rate and 12 kV charge voltage. The pulselength was 5 ns FWHM. We were unable to operate the laser at higher than 12 kV, due to high voltage breakdown. Even at this relatively low voltage, the average power was acceptable. The pulse length was shorter than desired, but most importantly, the laser was not reliable. Both the self-triggered spark gap, and the areas where the transmission lines connected to the gap and laser tube needed repeated servicing. This was a tedious process and destroyed the alignment of the N_2 laser to the dye laser system. Despite the improvement of this laser over the Blumlein devices described above, the laser had to be abandoned due to lack of reliability.

The N_2 laser employed in our experiment successfully overcame the faults of the previous designs. It is an adaptation of a design by Woodward, et al.[54] The one meter long laser tube, shown in cross section in Fig. 3.5a, is constructed from two 12.7 mm Al sides housing 87 cm long triangular stainless steel electrodes. The electrodes were carefully machined and deburred to avoid any knicks or discontinuities, and the electrode tip was slightly rounded. This was to avoid the formation of a local high current arc in the tube that could eventually lead to failure. The side-plates ("spars") containing the electrodes were located

parallel to each other by two 1 meter long, 9.5 mm thick plates of Synthane-Taylor type G-10 (green) epoxy fiberglass which formed the top and bottom insulating walls of the laser tube. The electrode spacing of the assembled tube was 32 mm. The nitrogen was admitted through a pair of 6.3 mm nylon tube fittings located in the insulator walls at the center of the tube. A small U-shaped cap over each inlet hole acted to deflect the input gas flow towards the axis of the tube. This was done to minimize the local region of higher pressure at the tube center. The nitrogen was exhausted through four 19 mm tube fittings located at the ends of each spar. The spars were cooled by water flowing in 76 mm long sections of brass waveguide 10 × 20 mm in cross section, which were held to the tube with a series of clamps. Thermal heat sink compound filled any cracks between the water channels and the spars.

The end caps of the tube were machined from plexiglass. These served both as structural feet and mirror holders. The mirrors were an overcoated Al flat, and an uncoated quartz flat. They were aligned by squeezing the O-rings sealing the mirrors to the end caps while monitoring laser power and beam profile. The laser tube was assembled using RTV silicone cement. After many hundred hours of operation of the tube under the conditions below, the only degradation of the laser tube was some fraying of the fiberglass tube walls near the exhaust ports.

Figure 3.5b shows the schematic diagram of the N_2 laser. The dumping capacitor was a parallel connection of one hundred 122 cm long Belden YK-217 cables, arranged in parallel groups of fifty along the upper and lower edge of the discharge tube. As shown in Fig. 3.5a, the outer conductor of each cable was clamped to the left spar and the inner conductor to the right. On both ends of each cable, where the outer conduc-

tor shield was stripped back, the insulation was reinforced by a thin strip of Mylar inserted between the outer conductor and the cable's dielectric insulator. This helped prevent breakdown at the cable's most vulnerable point. The total capacitance of the cable transmission line was 44 nF, and since the characteristic impedance of YK-217 cable is 14.8 Ω, the inductance of the 100 cable assembly was ~ 1 nH.

The cables were supported in two places along their lengths by clamps holding their jackets and terminated by a dummy laser tube constructed of spars similar to those in the laser head, but separated by a number of thick plexiglass washers. One of these spars was connected directly to the massive Al structure forming the ground shield around cable termination, storage capacitor, and spark gap. The other floated within the structure and made contact with storage capacitor C_1.

The storage capacitor was a 0.5 μF, 30 kV model from High Voltage Components, Inc. The spark gap was similar to that used in Steven Chu's flashlamp-pumped dye laser.[61] The electrodes were made of Elkonite tungsten-copper alloy and were remachined when they became pitted. The spark gap was fired by discharging a ~ 10 kV pulse through a commercial spark plug with gap electrode removed. It was mounted in a central hole in the ground spark gap electrode. The trigger pulse was generated using an SCR to discharge a 500 V, .05 μF capacitor into the primary of an EG & G TR-136B trigger transformer. The spark plug was connected to the secondary. The spark gap was pressurized at 10 psig N_2. This N_2, after passing through a filter and needle valve, was used in the laser tube.

The spark gap could be operated for about 10^6 laser shots (20 hours at 15 Hz) before service was required. The N_2 pressure had to be gradually increased for reliable operation during this period. Service to

the spark gap then took about one hour and consisted of cleaning soot off the plexiglass spark gap housing, remachining the electrodes, and adding spacers under the electrodes to regain the nominal 3.5 mm spacing. The only other service ever required was removing failed cables. These were thrown away without replacement.

Figure 3.6a shows the laser tube pressure giving maximum output as a function of charge voltage. Figure 3.6b shows the laser average power, at optimum pressure, as a function of charge voltage and repetition rate.

Monitoring the laser output with a fast photodiode and Tektronix 519 oscilloscope showed the pulse to pulse stability to be better than 10% provided the laser was run at a pressure slightly lower than that which gave the maximum average power. The typical operating parameters of our N_2 laser were: charge voltage 17 kV, repetition rate 15 Hz, pressure 60-65 torr, and output 4 mJ/shot. The pulse was smooth, and of FWHM 7.5 ns.

3.2 THE DYE LASER SYSTEM

Our dye laser system is shown in Fig. 3.7. There are two independently tunable oscillators for the pump and probe beam. The pump oscillator is followed by two travelling wave amplifiers.

Both oscillators were of the Hänsch[62] design, Fig. 3.8. Each oscillator was pumped by ~ 75 kW from the N_2 laser, focused into 10 mm long active region AR of dye cell DC. The focusing by 75 mm fused silica cylindrical lens CL, and the dye concentration, 5×10^{-3} M Rhodamine 6G in ethanol were adjusted to make the transverse dimensions of AR approximately 120 × 120 μ. With no optical feedback present, the orientation of the dye cell is adjusted so that the bright, comet shaped spots of

amplified spontaneous emission emerging from either side of the dye cell are of the same shape and intensity. Then, front mirror W, an uncoated 3° wedged fused silica window , is placed at a distance d_1 = 50 mm from the dye cell and aligned to produce a broadband, near diffraction limited laser beam emerging from the opposite side. This beam is collected and magnified by a high quality telescope represented by lenses L_1 and L_2 in Fig. 3.8. The pump oscillator used a Spectra-Physics 334/336 telescope with lenses of effective focal lengths 8.5 mm (L_1) and 200 mm (L_2). The probe oscillator used a Molectron DL-020 Galilean telescope with a geometric magnification of 22.5.

The magnification, and concomitant reduction in beam divergence, is critical in the line-narrowing of the laser output. Using grating G in Littrow mount (retroreflection), the telescope focusing adjustment d_3 is carefully scanned for best laser output. Assuming a Gaussian beam distribution (a good approximation as verified by scanning the laser output with a knife edge), the beam diameter W_4 at the telescope output is given by

$$W_4 = \frac{f_2}{f_1}\left[W_1^2 + (d_2 - f_1)^2\left(\frac{\lambda}{\pi W_1}\right)^2\right]^{\frac{1}{2}}, \qquad (3.1)$$

where f_1 and f_2 are the focal lengths of the lenses, W_1 is the beam waist in the dye cell, and d_2 is the distance between L_1 and the dye cell (Fig. 3.8). Note that the contribution from diffraction, the second term within the brackets in Eq. (3.1), is comparable in size to the first term, which is the geometric optics result. For W_1 = 60 μm, λ = 590 nm, d_2 = 75 mm, f_2 = 200 mm, and f_1 = 8.5 mm, Eq. (3.1) predicts W_4 = 5.1 mm and $\Delta\theta_4 = \lambda/\pi W_4$ = 37 μr. The dispersion of the diffraction grating in

Littrow mount is given by

$$\frac{d\lambda}{d\theta} = \frac{\lambda}{2\tan\theta} \tag{3.2}$$

leading to linewidth (FWHM)

$$\Delta\lambda \approx \frac{\lambda^2}{\pi W_4 \tan\theta} . \tag{3.3}$$

In our lasers, we used an echelle grating having 625 lines/mm and a blaze angle of 61° 10' (Bausch and Lomb 35-63-05-720). At 590 nm, we operated in the fifth order, at an incident angle of 67.2°. Under these conditions, Eq. (3.3) preducts a linewidth of .09 Å or 8 GHz. This was roughly verified by viewing the Fabry-Perot ring pattern formed by an etalon, Molectron DL-026C, having free spectral range 34 GHz and finesse 20.

Further line-narrowing of the pump and probe oscillators was achieved by inserting a Fabry-Perot etalon between grating and telescope. The pump oscillator, whose frequency was not varied during a data run, contained a solid etalon of FSR 20.5 GHz and finesse of 15 (Burleigh SE-5). This limited the pump bandwidth to ~ 1 GHz. The probe oscillator contained an air-spaced etalon (Burleigh FG-7) to facilitate pressure scanning. The free spectral range was 15 GHz and the finesse was 13. The probe bandwidth was also ~ 1 GHz. Both oscillators were linearly polarized by insertion of Glan-Thompson prisms between output coupler and dye cell.

The pump oscillator was amplified by a two-stage travelling wave amplifier.[63] The first amplifier, ADC_1, was a trapezoidal cuvette pur-

chased from Precision Cells, Inc. The second amplifier, ADC_2, was a home-made transversely pumped flowing dye cell identical to those used in the oscillators. The dye solutions were 5×10^{-3} M R6G in ethanol.

Referring to Fig. 3.7, the pump oscillator light was collimated by 80 mm f.l. lens L_1 after passing through mode clean-up aperture A. For some experiments, the light was passed through optional Pockel cell PC; see section 3.3. The light was then focused by 75 mm f.l. lens L_2 into ADC_1, where it was met with approximately 100 kW of suitably delayed N_2 pump light. Fifty mm lens pair L_3 and L_4, separated by dispersive direct view prism DVP, and followed by 100 μm pinhole PH, acted as a low dispersion spectrometer to remove amplified spontaneous emission from the output of the first amplifier. The beam was collimated by 80 mm f.l. lens L_5, turned by an Al mirror, and passed through Glan-Thompson polarizer P_3 for polarization state clean-up. L_5 also served to focus the light into final amplifier ADC_2, pumped with 200 kW of N_2 laser light. The final output was a slightly elliptical diffraction-limited beam of 70-100 μJ per shot in a 5 ns FWHM pulse. Due to saturation in the amplifiers, the ± 15% fluctuation in the pump oscillator is reduced to ± 5% at the amplifier chain output. Amplified spontaneous emission was less than 1%.

The probe laser was pressure scanned.[64] This was to assure uniform tuning rate and prevent misalignment of the probe beam as the spectrum was recorded. Pressure scanning was accomplished by mounting both grating and air-space etalon in a rigid pressure-tight box. The grating dispersion is given by

$$\frac{\lambda}{n} = \frac{2d}{M_G} \sin\theta_G; \tag{3.4}$$

the etalon dispersion is given by

$$\frac{\lambda}{n} = \frac{2h}{M_E} \cos\theta_E. \tag{3.5}$$

Evidently, wavelength will tune linearly with refractive index, provided the other variables in Eqs. (3.4) and (3.5) remain constant. It is most important that the input beam to the pressure box be perpendicular to the inside face of the window. Otherwise, as the pressure is scanned, the incident angle on grating and etalon change, and the differing sine and cosine dependences of Eqs. (3.4) and (3.5) cause the tuning elements to mistrack.

In our set-up, the pressure chamber base was a thick Al plate, 405 × 367 × 63 mm, and the optical elements, mounted in gimbal mounts, were attached to a 19 mm thick steel plate bolted to the base. Light was admitted through an AR-coated, $\lambda/10$, window with a 30 minute wedge mounted in a vacuum flange. Another flange was connected to a manifold through which nitrogen or propane could be leaked in through a needle valve or pumped away using a vacuum pump. An MKS 221 Baratron gauge capacitance manometer monitored the pressure between 0 and 1000 torr with 1 torr resolution and .1% linearity. An analog output drove the x-axis of an x-y plotter. The index variations are[64]

$$\text{Nitrogen: } n = 1 + 3.658 \times 10^{-7}\ p\ (\text{torr}) \tag{3.6}$$

$$\text{Propane: } n = 1 + 13.46 \times 10^{-7}\ p\ (\text{torr}). \tag{3.7}$$

These equations were used to calibrate our spectra. At 589 nm, 0 to 1000 torr nitrogen scan yields $\Delta\nu = -6.21\ \text{cm}^{-1} = -186.2$ GHz. Similar-

ly, a 0 to 1000 torr propane scan yields $\Delta\nu = -22.85\ cm^{-1} = -685.1$ GHz.

3.3 THE RIKES SPECTROMETER

Figure 3.9 shows our nonlinear optical spectrometer. Linearly polarized light from the probe laser was focused by 50 mm lens L_1 onto 50 μm pinhole PH_1. This aperture served as a fixed object point that was imaged into the sample and reimaged onto a spatial filter. The probe beam's diameter at PH_1 purposely overfilled the pinhole. This enabled a diffraction-limited beam to be relayed through the probe beam arm of the spectrometer independent of slight beam walk-off or misalignment of the probe laser when it was tuned. After passing through compensator C, aperture A_p removed the Airy rings diffracted from PH_1. The beam was then focused by 67 mm f.l. lens L_2 into sample cell SC located 100 mm from L_2. Analyzer A, a Glan-Thompson prism, was crossed with the polarizer in the probe laser cavity to form the optical Kerr effect set-up. Since the extinction of these two polarizers is the most important limitation on the signal to noise ratio, special effort was taken to minimize and compensate birefringence in the system. We chose .25 mm thick microscope slide covers as cell windows and glued them to a stainless steel cell body. This cell design had less birefringence than commercially produced cells tried. The cell itself was mounted on an x-y translation stage with adjustments in a plane perpendicular to the beam. This enabled us to search for the spots of least birefringence in the 10 mm clear aperture of the cell.

When the extinction was optimized by adjusting the analyzer and scanning the cell, compensator C was installed just in front of pinhole PH_1. This was a fused silica window, 25 mm in diameter by 10 mm thick,

held against a shallow step in a brass tube by a worm drive hose clamp.[65] The clamp was purposely tightened to induce an irregular strain field in the window as viewed through crossed polarizers. In this way, "every possible" waveplate was available when the brass tube was rotated and the aperture of the strained window scanned by translating the entire assembly perpendicular to the beam. By a painstaking search over the compensator's aperture and orientation, a factor of two to five improvement in extinction could be achieved. We estimate our extinction to be 10^{-6} to 5×10^{-7}. Once the point of best extinction was found it was quite stable.

After passing through the analyzer, the beam path was folded by a mirror which also served to block stray light from the pump beam. The signal beam was collimated by 150 mm lens L_3, passed through an aperture, and focused by 67 mm lens L_4 onto 50 μm spatial filter pinhole PH_2. This spatial filter was critical in rejecting the other major experimental noise source, scattered light from the pump beam. Placing a card in front of PH_2 in the darkened room, one could see a signal spot and various spots due to scattered pump light. It was important to align all the optics so that the signal spot was not overlapped by any of these noise spots. Then, PH_2 was positioned using an x-y translator to pass only the signal spot. After passing through filter stack FS, the signal was detected by an RCA 6342A photomultiplier tube.

The pump beam arm of the experiment was simpler. The near diffraction-limited output of the final amplifier was folded by a mirror, passed through a mica quarter wave plate for polarization selection, and focused by 80 mm L_5 into the overlap region of the cell. L_5 was located 90 mm from the focus in the cell and 530 mm from the final amplifier. It was

mounted on a precision x-y-z stage (Microswiss). This stage was used to perform the critical overlap of pump and probe beams in the cell. It was important that only adjustments on the pump arm be made once the probe beam extinction was optimized. The angle of intersection of the ~ 25 μm diameter laser beams in the sample cell was 4°, the estimated overlap length was .5 - 1 mm. Not shown in Fig. 3.9 were various masks in the cell region and detectors that monitored the pump and probe beams. These monitor beams were obtained from specular reflections off the sample cell windows and detected by EG & G SGD-100A silicon photodiodes.

The nonlinear signal, and pump and probe monitor signals were fed into gated electrometer circuits. After detection, the RIKES and probe signals were integrated with a 10 second time constant. An analog divider removed the probe dependence from the displayed signal. The pump beam intensity was constantly monitored to assure a power drift of less than 5% over the data run. Sometimes the unregulated N_2 laser power supply or the N_2 pressure was adjusted manually to compensate for pump beam power drift.

A data run consisted of evacuating the probe beam pressure box and then letting the scan gas leak in from a gas tank and regulator. Solenoid valves controlled pressurization or evacuation, permitting the probe wavelength to be scanned up and down. The normalized nonlinear signal was fed to the y-axis of an x-y recorder; a signal from the Baratron gauge proportional to the absolute pressure, and hence probe wavelength, drove the x-axis of the recorder. Typical runs took 5-10 minutes to complete.

In the study of the Brillouin spectrum, it was necessary to controllably attenuate the pump beam to record the dependence of the spectrum

on pump power. Absolutely no change in alignment could be tolerated, ruling out the use of neutral density filters. The variable attenuator consisted of Pockel cell PC preceeding the first amplifier, in conjunction with polarizer P_3 (Fig. 3.8). Changing the voltage across PC and subsequent analysis by P_3 permitted variable attenuation without either misalignment or change in polarization state.

Figure Captions

Fig. 3.1 Nitrogen laser discharge circuits.

(a) Blumlein laser

(b) "Capacitor-transfer" laser

Fig. 3.2 Cross sections of single- and dual-plane Blumlein nitrogen lasers. The dark layers between the conductors are three sheets of .13 mm mylar insulation.

Fig. 3.3 Parallel-plate capacitor-transfer nitrogen laser.

Fig. 3.4 Performance of parallel-plate capacitor-transfer nitrogen laser at 12 kV charge voltage.

Fig. 3.5 Multiple-cable capacitor-transfer N_2 laser.

(a) Detail of laser tube cross section

(b) Schematic diagram

Fig. 3.6 Performance of multiple-cable N_2 laser.

(a) Nitrogen pressure giving best power vs. charge voltage

(b) Average power vs. charge voltage

Fig. 3.7 Narrow-band, dual frequency tunable dye laser system.

Fig. 3.8 Hänsch type dye oscillator.

Fig. 3.9 RIKES spectrometer.

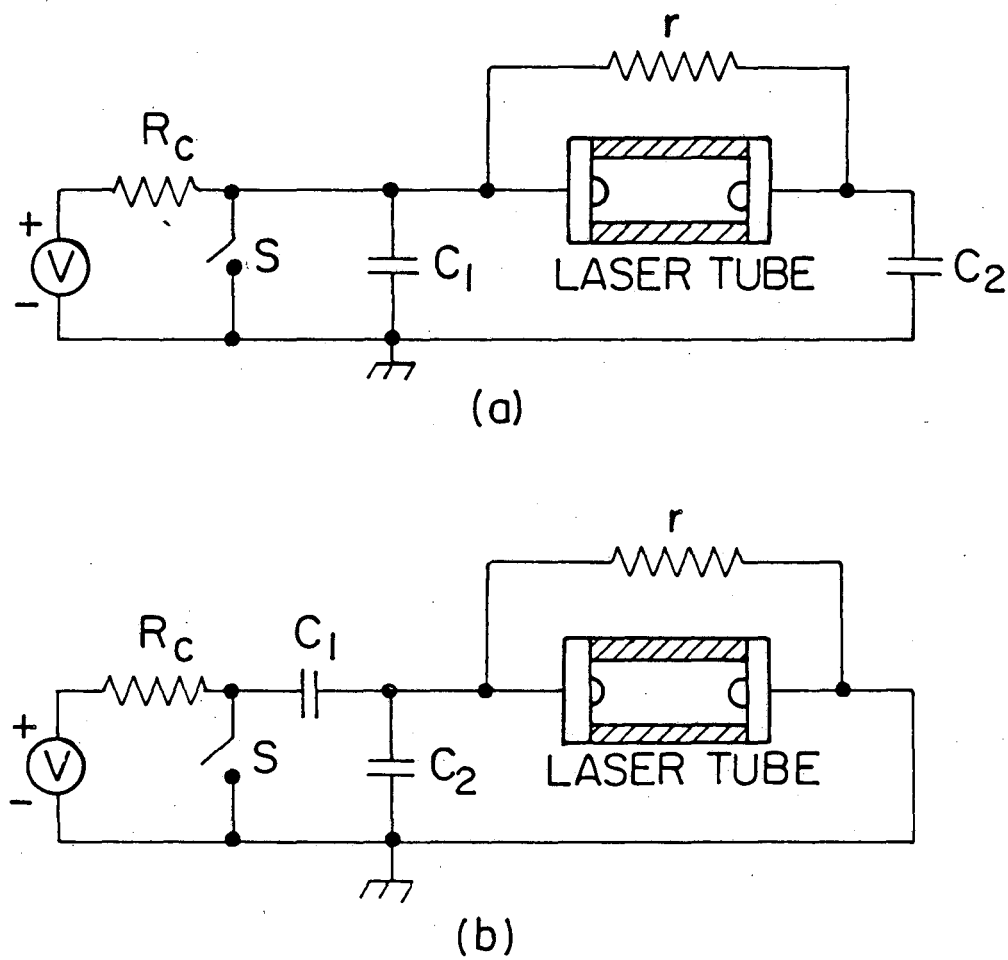

Figure 3.1

XBL823-5338

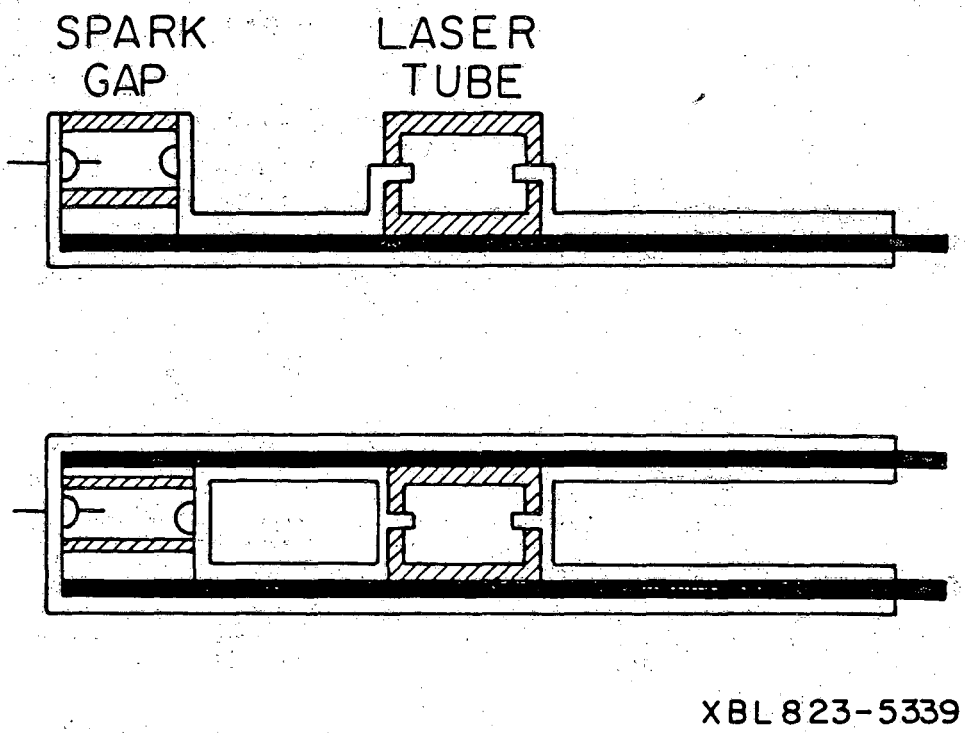

Figure 3.2

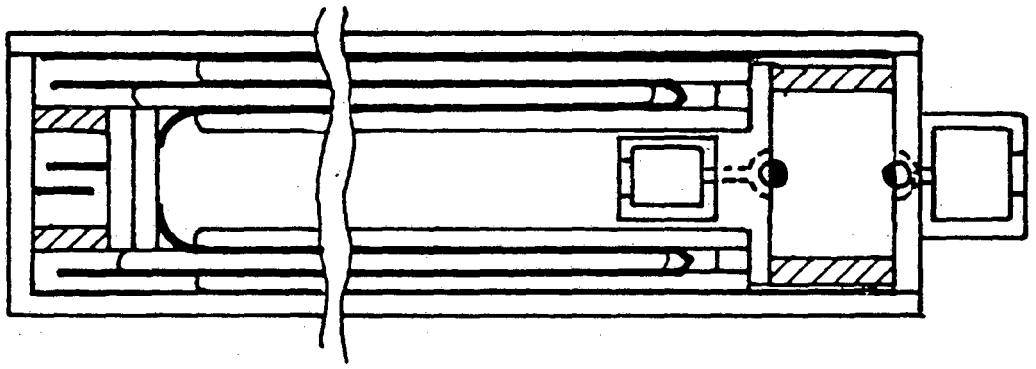

XBL823-5340

Figure 3.3

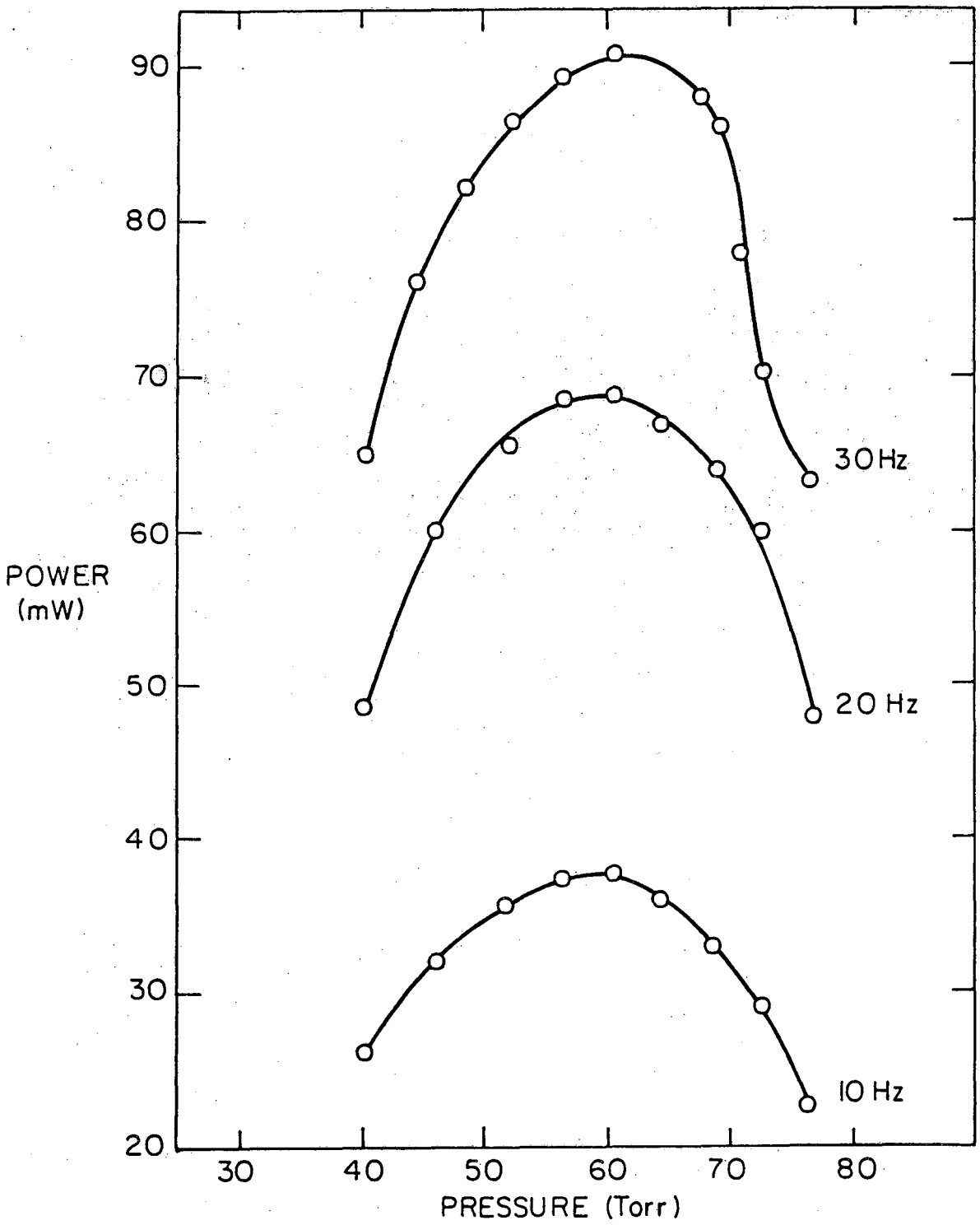

Figure 3.4

XBL 823-5341

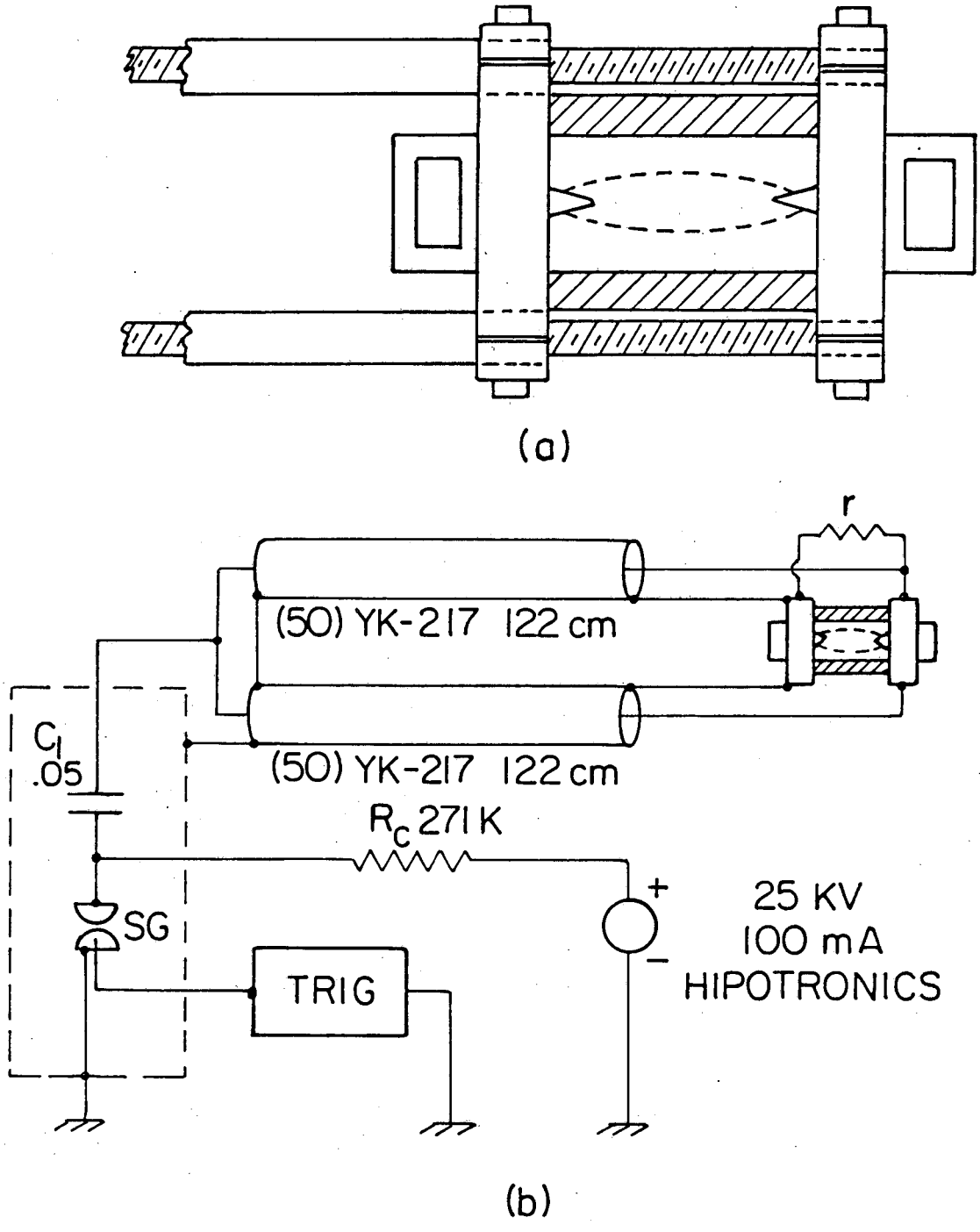

XBL 823-5342

Figure 3.5

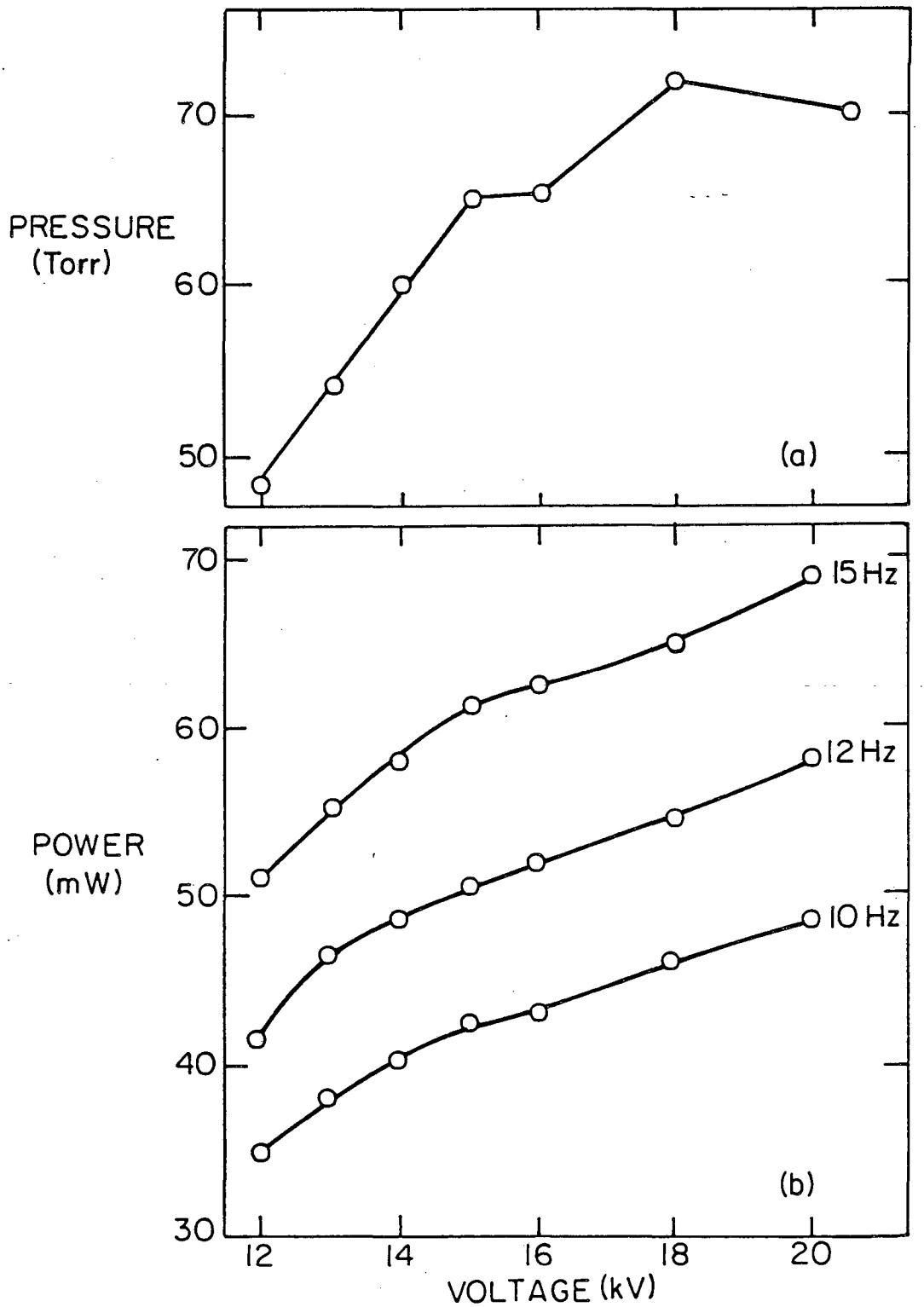

XBL 823-5343

Figure 3.6

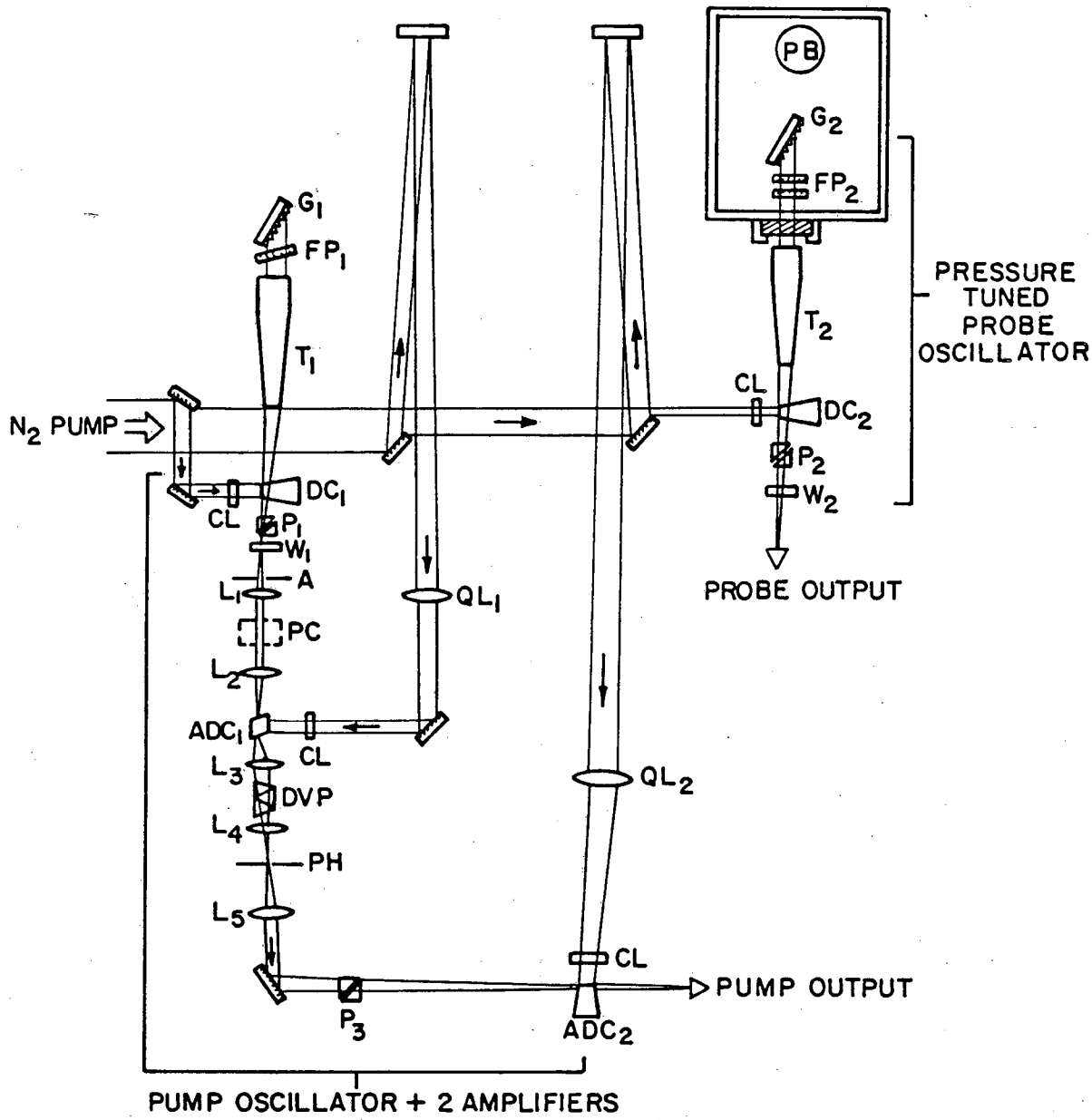

NARROW-BAND, DUAL FREQUENCY, TUNABLE DYE LASER SYSTEM

XBL 7812-6323

Figure 3.7

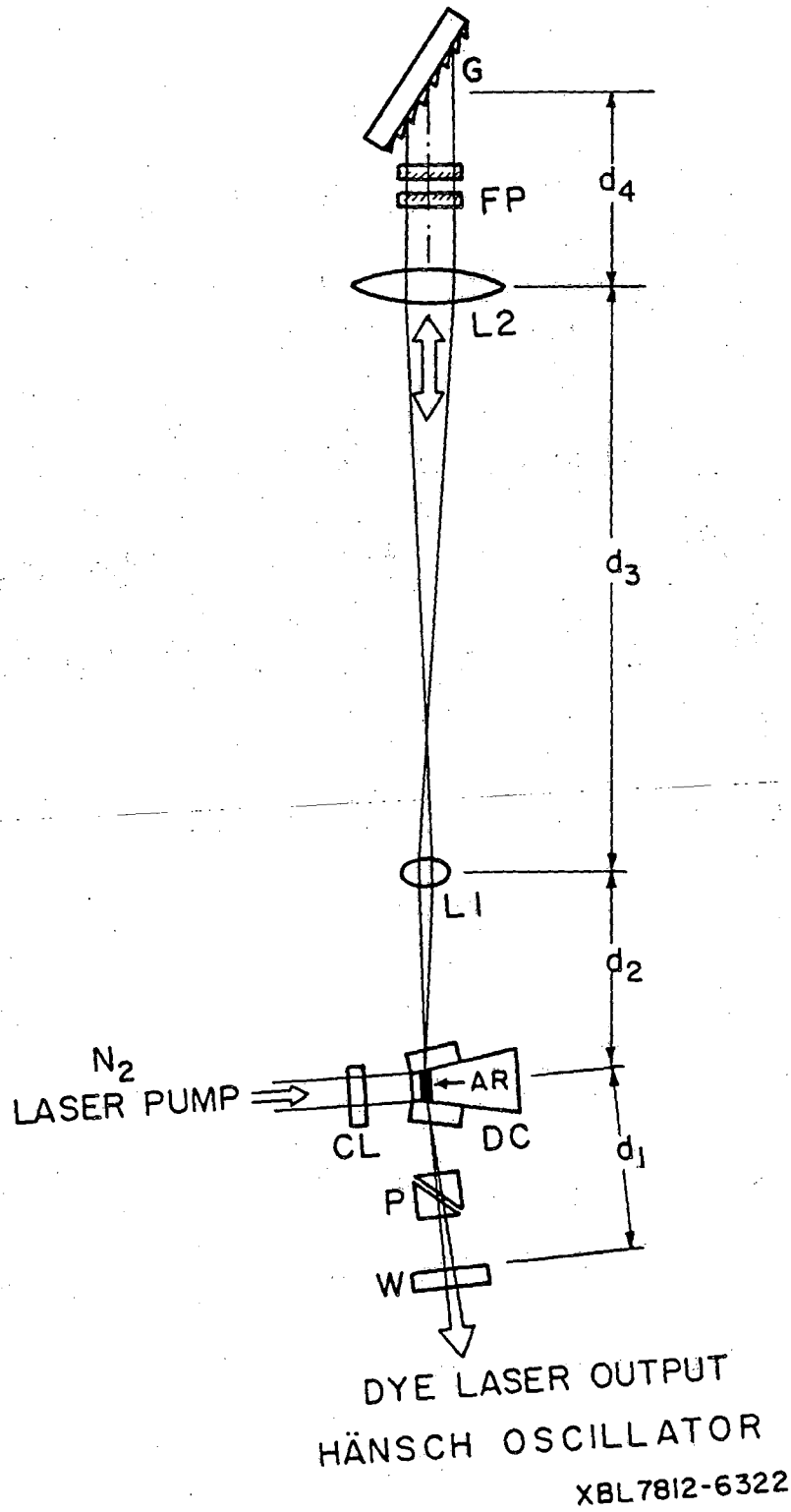
G
FP
d_4
L2
d_3
L1
d_2
N_2
LASER PUMP
AR
CL
DC
d_1
P
W
DYE LASER OUTPUT
HÄNSCH OSCILLATOR
XBL7812-6322

Figure 3.8

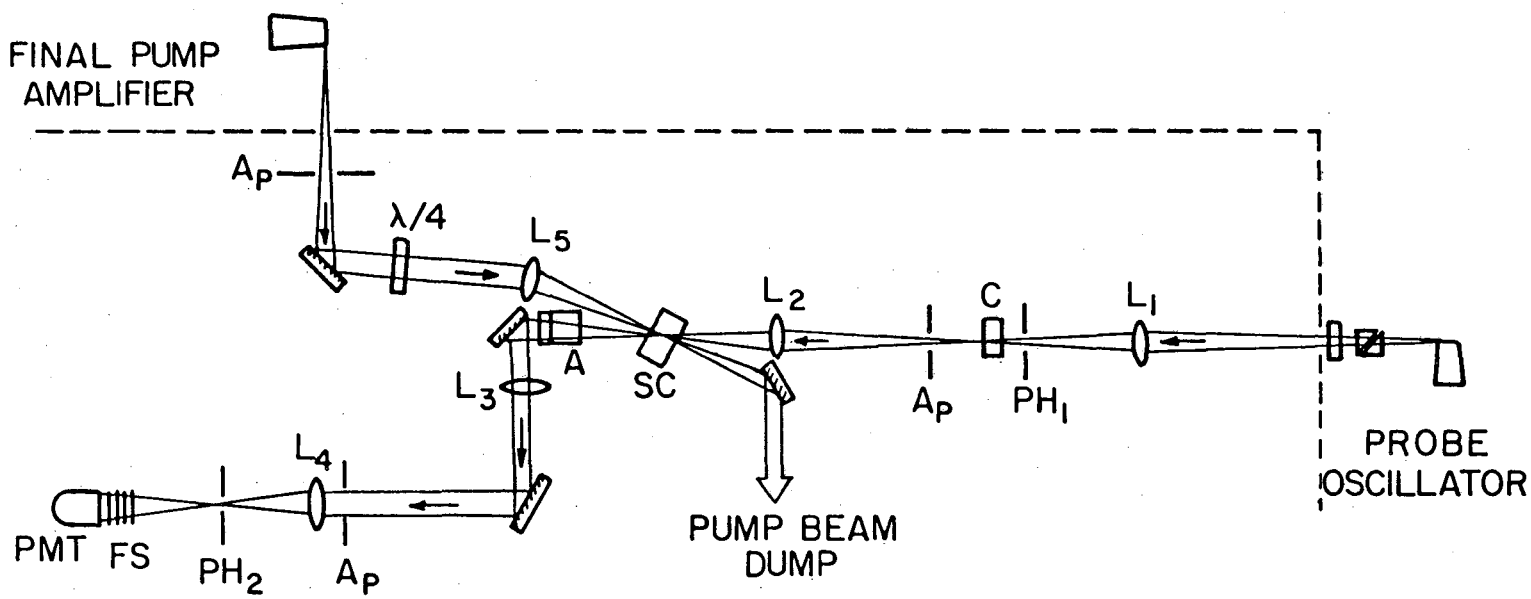

"RIKES" SPECTROMETER

Figure 3.9

XBL 7812-6324

4. RESULTS, INTERPRETATION, AND SUGGESTIONS FOR FUTURE WORK

4.1 THE BRILLOUIN SPECTRUM

The solid curve in Fig. 4.1 shows the Brillouin spectrum of CS_2 using the RIKE scheme. The pump frequency was $\Omega = 16980\ cm^{-1}$. The measured Brillouin shift $\omega_B = .23\ cm^{-1} = 6.9$ GHz agrees with the calculated value. The lineshape is dominated by the linewidths of the pump and probe lasers.

From the experimental traces, it is evident that as the pump power is increased, the Stokes peak grows more rapidly than the anti-Stokes peak. Previous to this investigation, RIKES spectra of Raman samples had always been analyzed with the parametric approximation given by Eq. (2.29); this model predicts equal Stokes and anti-Stokes peak heights. Evidently, the nonlinear polarization in our case is sufficiently strong that the effects of Stokes gain and anti-Stokes loss are enmeshed in the spectra of Fig. 4.1.

The spectra of Fig. 4.1 were obtained using nitrogen as the scan gas. In going from uppermost to the lowermost spectrum, the pump intensity was varied by varying the voltage on the Pockel cell (PC in Fig. 3.7). The light from the second amplifier cell was elliptically polarized. Polarizer P3 then stripped away energy in the wrong polarization state. Thus, the attenuation of the pump beam and the pressure scanning of the probe beam assured no change of alignment or beam profile, which was critical in assuring that only pump intensity is varied in this series of spectra.

To analyze the data, we use the general steady-state plane wave solution of the stimulated Raman scattering problem given in Sec. 2.3.

The polarizers had a high enough extinction that local oscillator effects were negligible; this could be verified by the symmetry of the circularly polarized Rayleigh-wing spectrum discussed below. Therefore, we use Eqs. (2.20) to (2.22), with $\mathcal{E}_{xo}(\omega) = \mathcal{E}_o$; $\mathcal{E}_{yo}(\omega) = 0$, and the signal $S = |\mathcal{E}_y(\omega,z)|^2$. For a linearly polarized pump beam, h = 1 and we obtain

$$S = |\mathcal{E}_y(\omega,z)|^2 = \frac{|\mathcal{E}_o|^2}{2}\{\exp[-2\gamma z\mathrm{Im}(\chi_A)]\{\cosh[2\gamma z\mathrm{Im}(\chi_B)] - \cos[2\gamma z\mathrm{Re}(\chi_B)]\}\} \tag{4.1}$$

where

$$\chi_A = \chi_{1111} + \chi_{1122} \tag{4.2a}$$

$$\chi_B = \chi_{1111} - \chi_{1122} \tag{4.2b}$$

and the intensity-dependent parameter γ is given by

$$\gamma = (6\pi\omega/\varepsilon^{\frac{1}{2}}c)|\mathcal{E}(\Omega)|^2 \propto I(\Omega). \tag{4.3}$$

For the nonlinear susceptibilities, we used the expression for electronic, orientational, and Brillouin contributions stated in Chap. 1:

$$\chi_{1111}(\omega = \omega + \Omega - \Omega) = \frac{1}{24}\left[3\sigma + \frac{4}{3}\,b(0)\,\frac{1}{1 + i\Delta\tau}\right] + \frac{G\,2\Gamma\omega_B}{\omega_B^2 - \Delta^2 + 2i\Gamma\Delta} \tag{4.4}$$

$$\chi_{1122}(\omega = \omega + \Omega - \Omega) = \frac{1}{24}\left[\sigma + b(0)\left(-\frac{2}{3} + \frac{1}{1 + i\Delta\tau}\right)\right] \tag{4.5}$$

where

$$\Delta = \Omega - \omega, \tag{4.6}$$

$$\omega_B = \frac{2nv}{c}(\omega + \Omega). \tag{4.7}$$

Because the experimental lineshapes were dominated by the lineshapes of the lasers, our data was not accurate enough to obtain the values of all the parameters in Eqs. (4.1), (4.3), (4.4), and (4.5). Rather, we chose to fit the spectra using the peak Brillouin susceptibility G, the linewidth Γ, and the pump intensity-dependent variable γ as adjustable parameters. For the parameters σ and b(0), we used the values $\sigma = 5.8 \times 10^{-13}$ esu, $b(0) = 4.95 \times 10^{-12}$ esu, based on an average of the recommendations of Owyoung, and Levenson and Song, discussed in Sec. 1.6. For the Brillouin shift ω_B, we used the value .23 cm^{-1}, calculated from the hypersonic velocity[27] $v = 1.26 \times 10^5$ cm/sec, the index of refraction n = 1.62, and the wavelength, 590 nm. The pump intensity parameter was then stepped, in arbitrary units, proportional to the measured power, and G and Γ adjusted to fit the peak heights of the Stokes and anti-Stokes peaks and the experimental lineshape. The dashed curves in Fig. 4.1 show the theoretical fit obtained using the values $G = 5.3 \times 10^{-12}$ esu and $\Gamma = .045$ cm^{-1}. The fitted value of the peak Brillouin susceptibility G is 20% lower than the value calculated from the spontaneous cross section measurement of Kato and Zdasiuk,[27] $\chi_{peak} = 6.5 \times 10^{-12}$ esu, as discussed in Sec. 1.6. The experimental linewidth $\Gamma = .045$ cm^{-1} is lower than the value .082 cm^{-1} estimated by summing the bandpasses of the etalons in the laser cavities. Evidently, the effect of multiple passes

through the etalons reduced the laser linewidths, which were not measured independently.

Our experiment was effective in demonstrating the technique of coherent Brillouin spectroscopy and in showing that one must carry the theoretical interpretation of RIKES spectra further than the parametric approximation when the pump intensity is high. We will discuss below experiments that will yield more accurate lineshapes, Brillouin susceptibilities, and exploit the Brillouin resonance in phase conjugation.

4.2 THE RAYLEIGH-WING SPECTRUM

The nonlinear signal due to field-induced molecular reorientation is weaker than that due to the Brillouin peaks and extends over a broader spectral range. Using the arguments of Secs. 1.3 and 1.6, we predict a peak $\chi_{1111} = \sigma/8 + b(0)/9 = 6.2 \times 10^{-13}$ esu, one order of magnitude smaller than the peak Brillouin susceptibility. The lineshape of the RIKES spectrum exhibits a complicated variation with the polarization of the pump beam. Because of the slow fall off characterizing Lorentzian spectra, it is desirable to take spectra over as broad a spectral range as possible. With our set-up, we were limited to a scan of 20 cm^{-1} using propane gas to pressure scan the grating and etalon of the probe beam.

Considering just the orientational and electronic contributions to $\chi^{(3)}$, we have

$$\chi_{1122}(\omega = \omega + \Omega - \Omega) = \frac{1}{24}\left[\sigma - \frac{2b(0)}{3} + \frac{b(0)}{1 + i\Delta\tau}\right] \tag{4.8a}$$

$$\chi_{1221}(\omega = \omega + \Omega - \Omega) = \frac{1}{24}\left[\sigma + b(0) + \frac{b(0)}{1 + i\Delta\tau}\right] \tag{4.8b}$$

$$\chi_{1212}(\omega = \omega + \Omega - \Omega) = \frac{1}{24}\sigma + b(0) - \frac{2}{3}\frac{b(0)}{1 + i\Delta\tau} \tag{4.8c}$$

where $\Delta = \Omega - \omega$. We found that, unlike the Brillouin spectra, the parametric approximation was adequate to explain the spectra. Therefore, we used the function

$$S = |E_y(\omega)|^2 \propto |(a^2 - b^2)\sin 2\psi(\chi_{1212} + \chi_{1221}) + i2ab(\chi_{1212} - \chi_{1221})|^2 \tag{4.9}$$

as explained in Sec. 2.3. To study the polarization dependence, four polarization states of the pump beam were used. These were generated by a quarter waveplate in the orientation of Fig. 4.2. If the pump is represented by $\vec{\mathcal{E}}(\Omega)$ before the waveplate, than after passing through it, it is altered to

$$\vec{\mathcal{E}}'(\Omega) = \hat{x}'[\hat{x}' \cdot \vec{\mathcal{E}}(\Omega)] + i\hat{y}'[\hat{y}' \cdot \vec{\mathcal{E}}(\Omega)]. \tag{4.10}$$

For an initially linearly polarized pump beam at 45° to $\hat{x}$, ψ is just the rotation of the fast axis $\hat{x}'$ from $\hat{x}$. The other parameters $h = (a^2 - b^2)\sin 2\psi$, and $f = 2ab$ may be shown to be

$$h = \sin^2 2\psi \tag{4.11}$$

$$f = \cos 2\psi. \tag{4.12}$$

Data was taken at $\psi = 0$, 22.5, 45, and 67.5 degrees corresponding to circular, elliptical, linear, and elliptical polarization states, respectively. The resulting pump polarization parameters are summarized in

Table 4.1.

Figures 4.3 through 4.6 show the experimental and calculated Rayleigh-wing spectra. Reference to Eq. (4.8) and (4.9) shows that the spectra are well described by the interference of the complex Lorentzian term with the real background due to the nonresonant Kerr, and electronic susceptibilities. No attempt was made to include the Brillouin susceptibilities in the calculations for two reasons. First, there were indications that the detection electronics were saturated when the probe beam was tuned to the Brillouin resonances. Second, the replacement of the Brillouin linewidth by the laser linewidth was not adequate in explaining the detailed lineshape produced by the interference of the Brillouin and Rayleigh contributions. Hence the spectra and calculations of Figs. 4.3 through 4.6 are valid only for $|\Delta| = |\Omega - \omega| \geqslant 1\ \mathrm{cm}^{-1}$. For these spectra, the values $\sigma = 5.8 \times 10^{-13}$ esu, $b(0) = 4.95 \times 10^{-12}$ were used, as in the fitting of the Brillouin spectra, and we used $\tau = 2.0$ psec for the relaxation time.

To study the spectral lineshape more closely we made a separate data run with a circularly polarized pump beam, Fig. 4.7. For this spectrum, our theory predicts

$$S_{cp} \propto |\chi_{1212} - \chi_{1221}|^2 \propto \left|\frac{b(0)}{1 + i\Delta\tau}\right|^2 \propto \frac{1}{1 + \Delta^2\tau^2} \qquad (4.13)$$

where we have again ignored the Brillouin peaks. The open circles were calculated using a pure Lorentzian with $\tau = 2.0$ psec. Near the Brillouin peaks, the detector was purposely blocked to avoid saturation. A constant background was also present in the fit of Fig. 4.7 to account for electronics noise. Our result for the relaxation is in agreement with

Table 4.1 Parameters of Pump Beam Polarization Ellipse

ψ	0°	22.5°	45°	67.5°
$f = \cos 2\psi$	1	$1/\sqrt{2}$	0	$-1/\sqrt{2}$
$h = \sin^2 2\psi$	0	1/2	1	1/2
polarization	circular	elliptical	linear	elliptical

the results τ = 1.96 psec from the spontaneous Rayleigh-wing measurement of Shapiro and Broida[66] and $\tau = 2.1 \pm 0.3$ psec from the Kerr gate experiments of Ippen and Shank.[67] However, our fit is not good enough to differentiate between those measurements and the scan range not great enough to discern the large detuning behavior of the susceptibility.

4.3 SUGGESTIONS FOR FUTURE WORK

In this work, we established that low frequency light scattering mechanisms are studiable by coherent Raman methods in a straightforward way. Work should now proceed to accurately measure lineshape functions and determine absolute cross sections by coherent Raman technique.

4.3.1 BRILLOUIN GAIN SPECTROSCOPY

The intrinsic high-resolution capabilities associated with coherent techniques should find good use in high resolution measurements of the Brillouin lineshape. Equation (2.27) shows that for 500 mW pump power, and CS_2 Brillouin susceptibility of 6.5×10^{-12} esu, the gain is a large .7%. This large gain, and the use of commercial CW dye lasers of linewidth 1 MHz suggest that the Brillouin resonances may be studied with a signal to noise ratio of 1000. Dividing the linewidth of the resulting gain spectrum by the signal to noise, we see that the Brillouin shift is measurable to a few kHz. At 590 nm, the Brillouin shift is 6.9 GHz. Thus we can measure the quantity [nv], where n is the refractive index and v the hypersonic velocity, to an accuracy of 10^{-6}. Of course, the gain technique may be applied to the Brillouin spectroscopy of other materials, provided a high optical quality sample is obtainable. The signal to noise ratio will scale as the Brillouin cross

section. If one is willing to accept a resolution of 100 MHz, one may use transform-limited dye laser pulses to induce the gain. Highly damped and very weak Brillouin modes should be readily detectable; the factor limiting these experiments is the Brillouin gain available when the pump pulses reach the damage threshold of the material.

Brillouin gain spectroscopy is also capable of providing a new and potentially highly accurate method of measuring the absolute Brillouin cross section. In spontaneous Brillouin scattering, absolute cross sections are measured by comparing the intensity of the Rayleigh scattering from a solution of spherical silica particles (LUDOX solution) with that of the Brillouin peaks.[27,28] The reference and sample channels are arranged about a central beamsplitter with utmost attention paid to the geometric symmetry of the two channels. The beamsplitter combines the signals, sending them to the analyzing Fabry-Perot interferometer. A combination spectrum results with the central Rayleigh peak from the LUDOX solution providing both the instrumental lineshape and absolute cross section reference. The latter is obtained by separately measuring the extinction coefficient of the LUDOX solution. In this technique, any uncorrected error in geometric symmetry, extinction measurement, and spectral deconvolution results in error. 10% accuracy is achievable.

Absolute gain measurements seem more straightforward with Brillouin gain spectroscopy. As mentioned above, the signal is strong. Reference to the discussion of Chap. 2 shows that the most critical element of this experiment is the measurement of the pump beam power inducing the gain; 2% accuracy should be achievable. The impressed gain on the probe can be accurately measured using a calibrated lock-in amplifier; the calibration can be made using an electrooptic modulator to simulate gain

or loss, or to null the nonlinear gain. Corrections to the gain formula (2.27) resulting from differing Gaussian profiles, finite cell length, etc., may be calculated and applied with confidence since measurements on the pump and probe beams are straightforward. Finally, the use of single frequency lasers eliminates the need for deconvolution operations, and the absolute cross section at each point of the spectrum is measured as the spectrum is scanned. An accuracy of 2% seems possible and, as we discuss below, the gain technique is well adapted for the intercalibration of the cross sections of different materials and different modes.

4.3.2 EXTENSIONS OF COHERENT RAYLEIGH-WING SPECTROSCOPY

It would be quite valuable to extend our knowledge further of the optical Kerr effect dispersion. Fortunately, since this investigation was completed, work has progressed in the field. Song et al.[68] have measured the gain spectrum of CS_2 for the Rayleigh-wing extending to $|\Delta\bar{\nu}| = 100\ cm^{-1}$. The resolution, $.7\ cm^{-1}$, did not resolve the Brillouin peaks. Both the polarized $Im(\chi_{1111})$ and the depolarized $Im(\chi_{1122})$ spectra were recorded. The principal new result of their investigation was the uncovering of a broad, weak Raman mode, of shift $35\ cm^{-1}$ and half-width $20\ cm^{-1}$, in the Rayleigh-wing. The mode appeared in the same proportion to the orientational contribution in both the polarized and depolarized spectra, and is believed to be due to molecular librations.[70]

To extend this work we recommend first that the absolute strength of the Rayleigh-wing scattering signal be measured. The parameter b(0) characterizing the orientational contribution can be obtained accurately from a high resolution Rayleigh-Brillouin gain spectrum spanning $\pm\ .5\ cm^{-1}$ about zero detuning. The absolute Brillouin cross section would

serve as the reference. Then, the results of ref. 68 can be used at once to deduce the absolute strengths of the exponential and librational contributions to the spectrum.

One further set of tests should be done. From our discussion of the orientational dispersion of the susceptibility, Eq. (1.36), and the tensor properties of the gain signal summarized in Eqs. (2.24a), (2.25), and Table 2.1, we predict that the ratio of Raman gains due to the orientational mechanism is [4:3:6:1] for [same linear:opposite linear:opposite circular:same circular] polarization configurations of pump and probe.[69] Owyoung's model of the librational contribution[70] obtains $b(t) = -3a(t)$ for the nuclear response functions. Therefore, he predicts that the polarization dependence of the orientational and librational contributions to $\chi^{(3)}$ are identical. Using Pockel cells in the pump and probe beams of a gain experiment, the four polarization states discussed above may be produced without alignment errors. The gain ratio predictions for both contributions may then be checked. As mentioned above, ref. 68 noted that the shape of the spectrum, and therefore the ratio of the orientational to librational contribution, remained unchanged for same linear and opposite linear polarizations of pump and probe. This result is consistent with Owyoung's model.

4.3.3 RAMAN CROSS SECTION MEASUREMENTS

The gain measurements described above will provide definitive data on the dispersion, cross sections, and symmetry of the low frequency light scattering mechanisms in materials. It is of course desirable to extend the measurements out in frequency to all the Raman modes of a material and thus completely characterize the light scattering spectrum.

Reference to the literature[71,72] shows that accurate absolute Raman cross section measurement by spontaneous scattering is an even more formidable task than the Brillouin measurements discussed above. Either the weak scattered intensity must be measured directly,[71] or it must be compared in intensity with radiation from a black body source.[72] In the latter measurement, the reference source emissivity and temperature must be known accurately. The instrumental response of the monochromator must be known precisely, and must be wider than the Raman line being studied. Then, a critical correction must be made for the difference in filling up the instrumental response by the broadband light source and the Raman resonance. Disagreements of 20% among workers are common.

Raman gain measurements, on the other hand, will not be much more difficult than the Rayleigh-Brillouin gain measurements discussed. Because pump and probe beam can now differ by $\gtrsim 1000\ cm^{-1}$, corrections to the simple gain results must be made for differing beam profiles for pump and probe. These are still quite straightforward. It would be desirable to be able to pump samples into and out of the sample cell without affecting alignment; inter-comparison between different samples could then be accomplished by just tuning the probe beam.

In conclusion we believe that by gain measurements, the entire light scattering spectrum of high quality, transparent samples is obtainable. We see that coherent techniques make possible the measurement of absolute cross sections, symmetries, and high resolution lineshapes with greater accuracy and convenience than spontaneous techniques.

Figure Captions

Fig. 4.1 Intensity dependence of RIKES Brillouin spectrum, CS_2. Experimental curve, solid line. Theoretical calculation, dashed line.

Fig. 4.2 Orientation of quarter-wave plate in pump beam.

Fig. 4.3 Theoretical and experimental CP Rayleigh-wing spectrum.

Fig. 4.4 Elliptically polarized pump spectrum. $\psi = 22.5°$.

Fig. 4.5 Linearly polarized pump spectrum.

Fig. 4.6 Elliptically polarized pump spectrum. $\psi = 67.5°$.

Fig. 4.7 Lorentzian fit (open circles) to CP Rayleigh-wing spectrum. $\tau = 2$ psec.

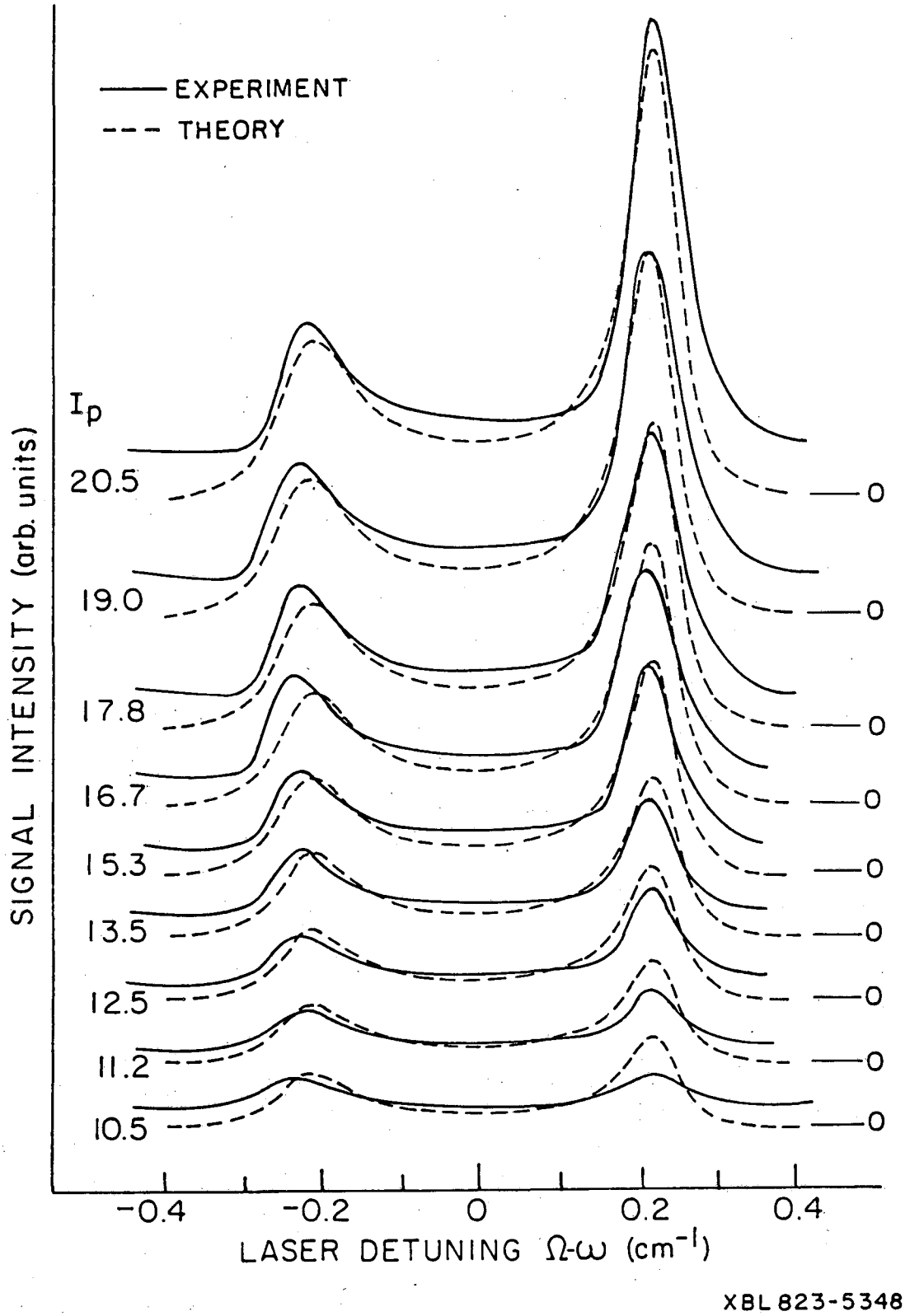
EXPERIMENT
THEORY
I_p
20.5
19.0
17.8
16.7
15.3
13.5
12.5
11.2
10.5
0
SIGNAL INTENSITY (arb. units)
-0.4
-0.2
0
0.2
0.4
LASER DETUNING Ω-ω (cm⁻¹)
XBL 823-5348

Figure 4.1

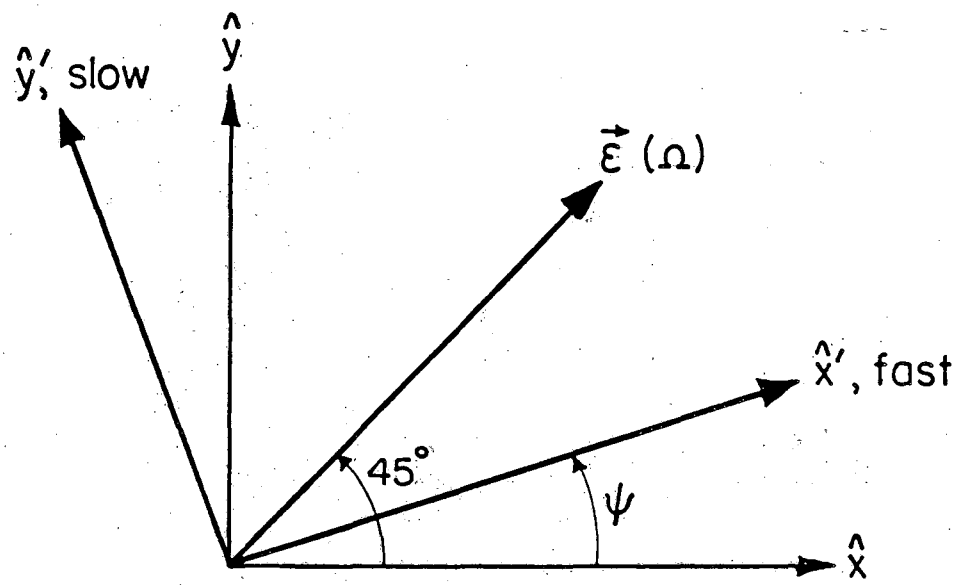

XBL823-5344

Figure 4.2

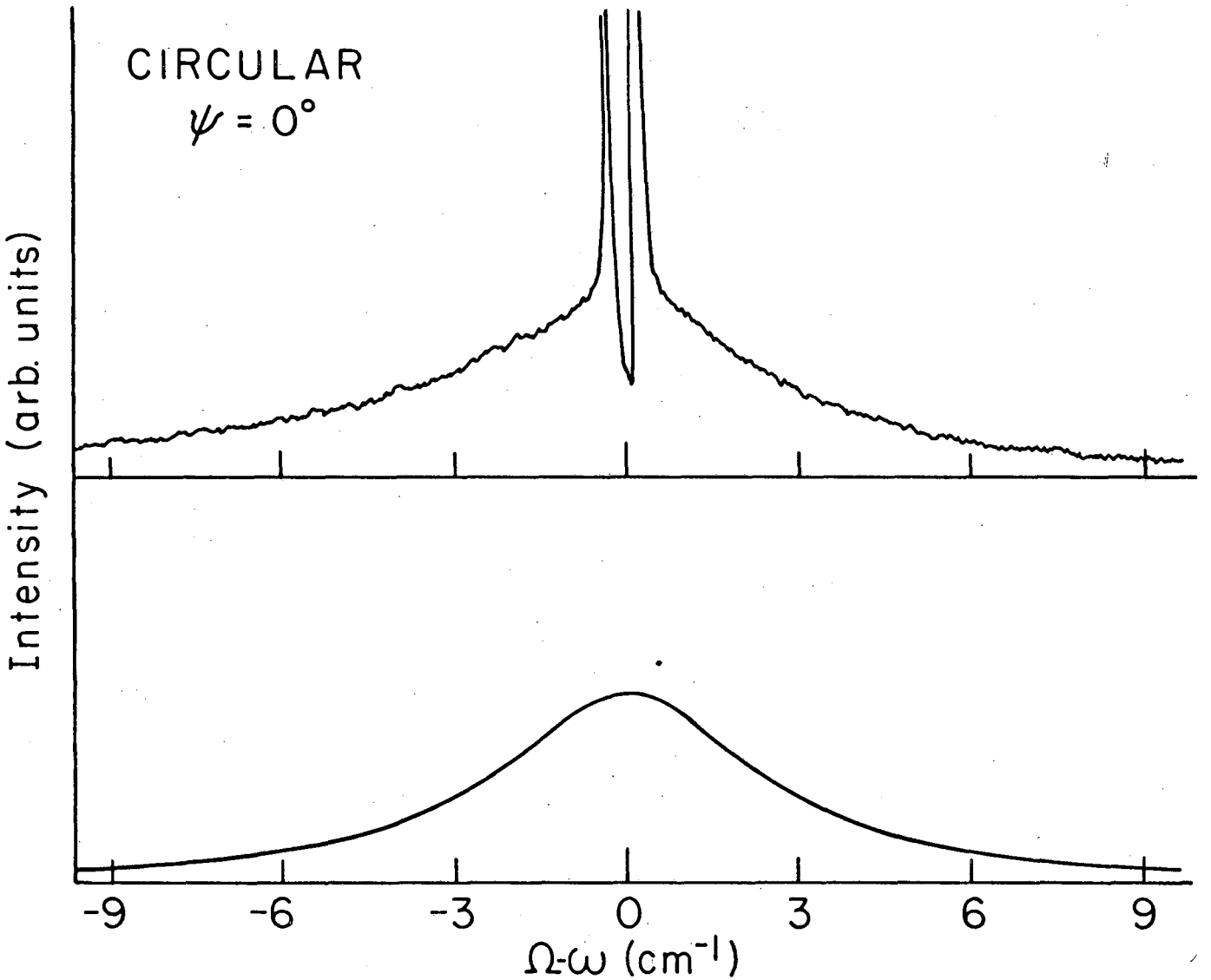

XBL 795-6202

Figure 4.3

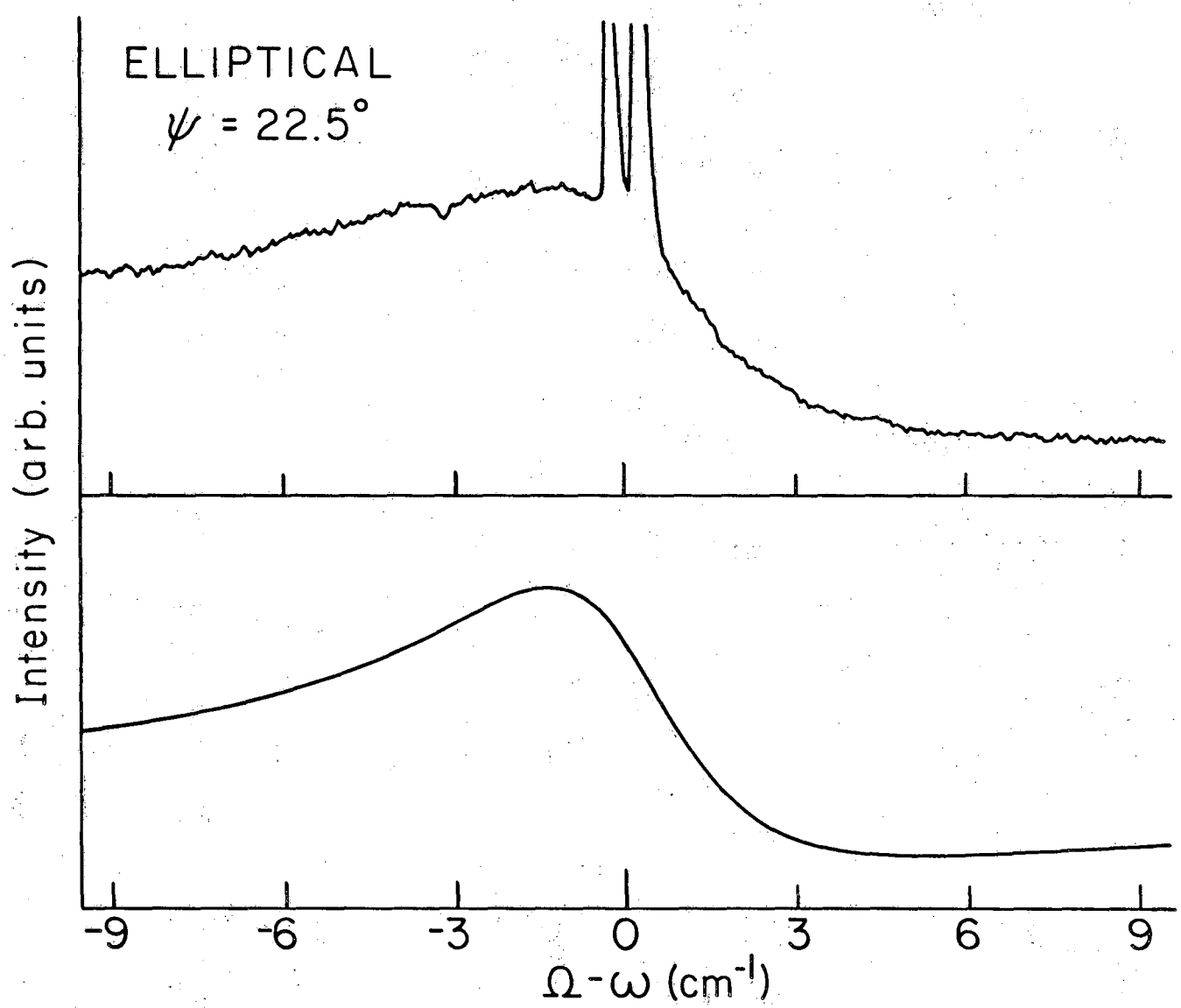

XBL795-6203

Figure 4.4

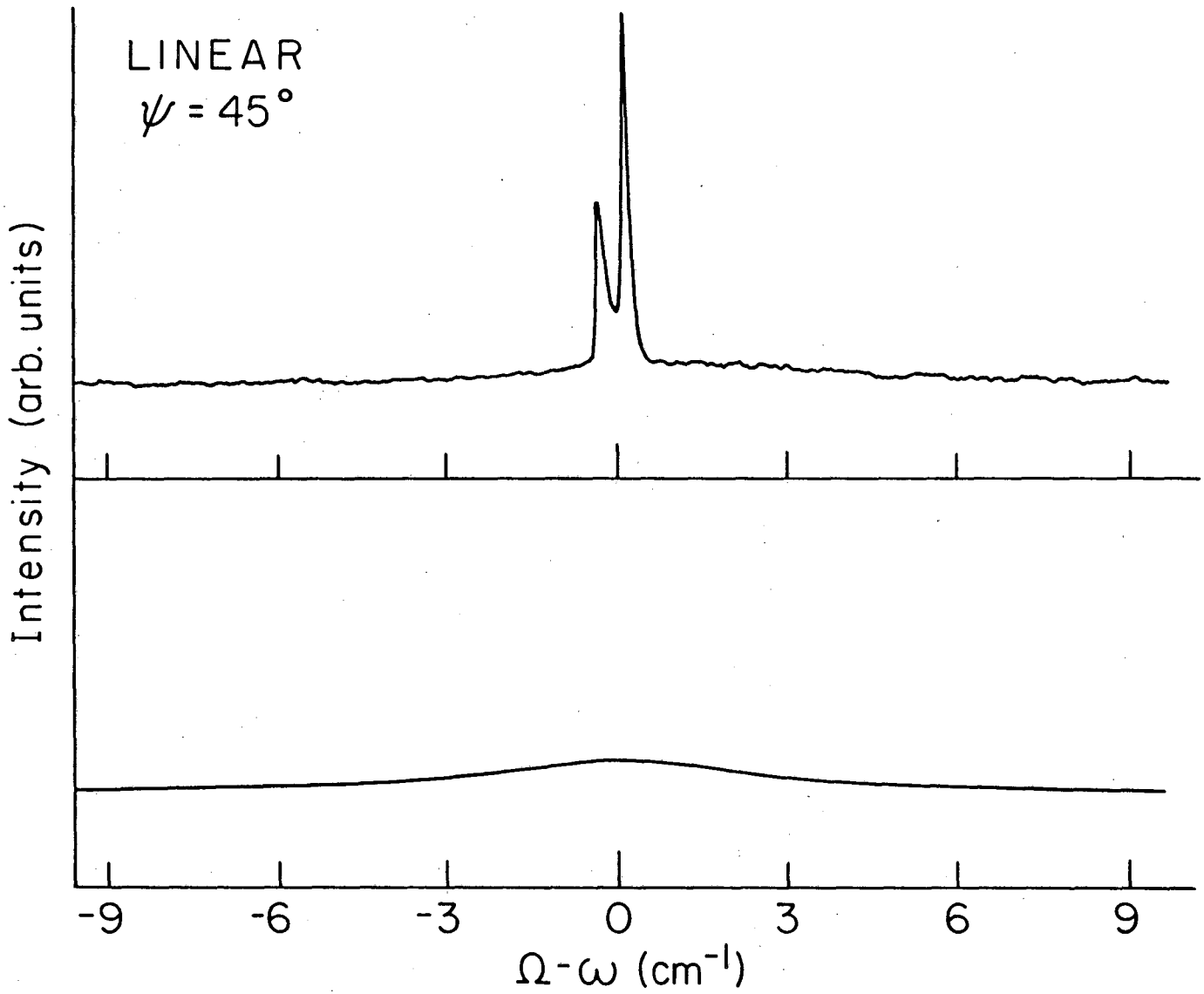

XBL795-6204

Figure 4.5

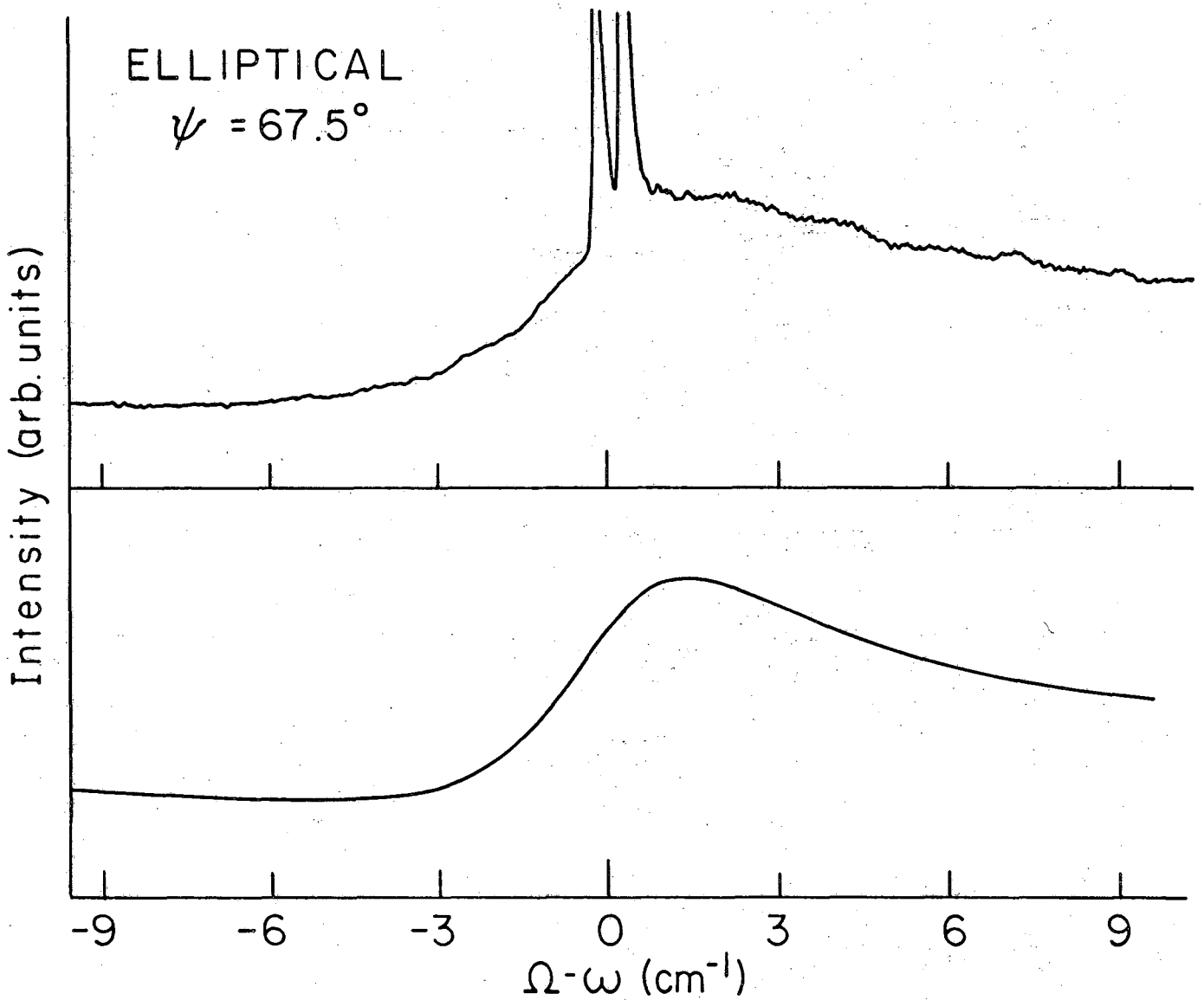

Figure 4.6

XBL795-6205

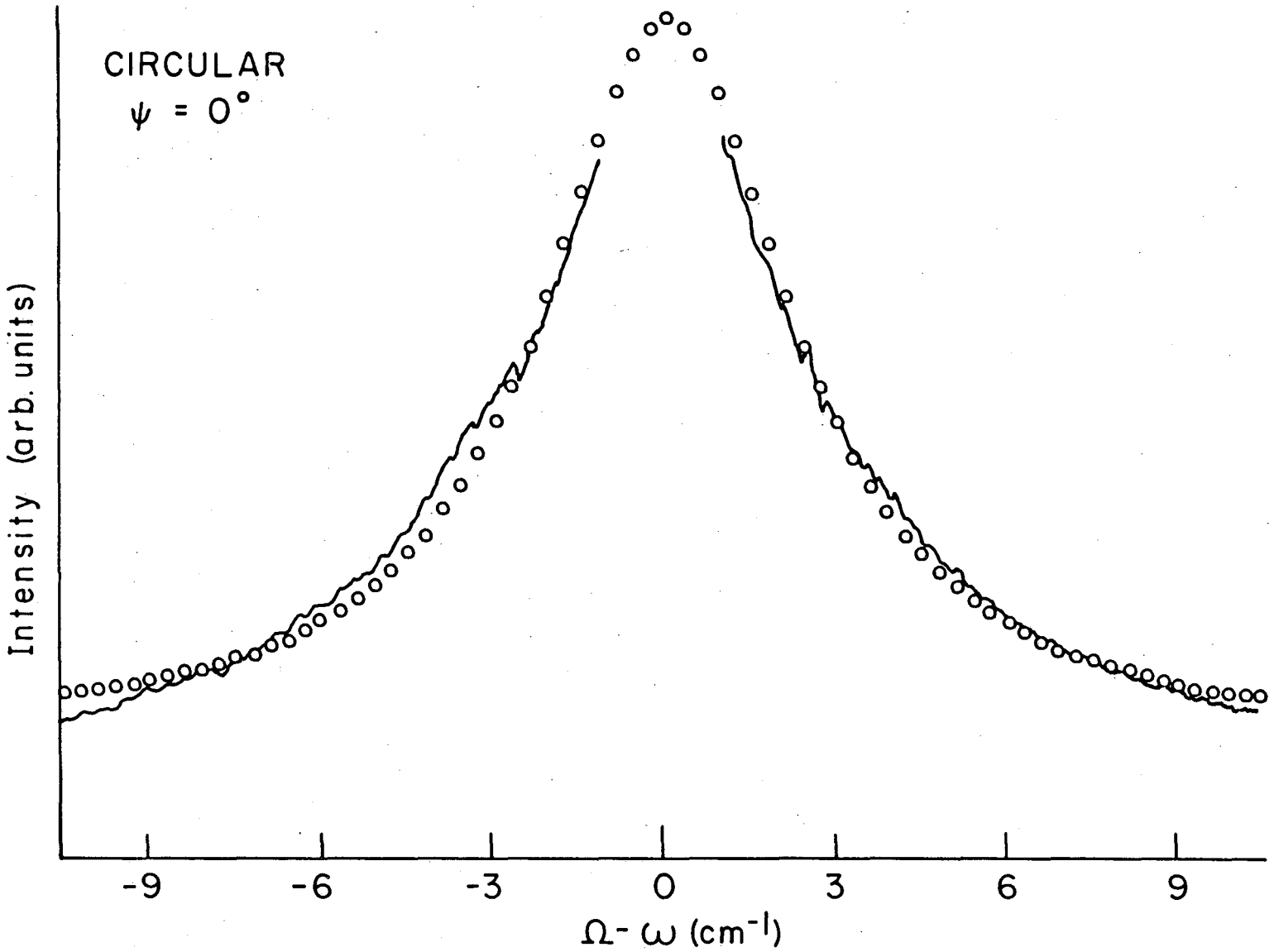

Figure 4.7

XBL 795-6206

5. A TUNABLE "BRILLOUIN MIRROR"

5.1 INTRODUCTION

In 1977, Hellwarth showed that a four wave mixing process could be used to generate a time reversed or phase conjugate replica of the wavefront of an arbitrary input monochromatic beam.[73] Yariv and Pepper showed that under strong enough excitation, this "phase conjugate mirror" (PCM) could reflect with gain, and that parametric oscillation could occur in a resonator formed by a PCM and an ordinary mirror.[74] A great many experiments followed, demonstrating the aberration correction, parametric gain, and oscillation properties of the degenerate four wave mixing process.[75-78]

It had meanwhile been long established that under certain conditions, the wavefront of backscattered stimulated Brillouin scattering is the phase conjugate of the pump laser wave.[79] This effect is preferentially observed when the pump laser has a spatially inhomogeneous transverse distribution due to poor beam quality or due to multimode excitation of the light guide containing the Brillouin medium. In this situation, it can be shown that the phase conjugate SBS wavefront has anomolously higher gain than other possible waves and thus gains ascendancy in the stimulated scattering process.[79-81] Subsequently, the phase conjugation by stimulated Brillouin scattering has been used in the construction of laser systems emitting high quality beams in the presence of aberrations.[82-84] Also, the conjugation of a wavefront incident at a small oblique angle to the axis of a cell in which SBS is occuring has been considered.[85-87] This process occurs due to the mixing of the weak incident probe wave with the counterpropagating pump and Stokes waves

participating in the SBS. Unlike the case of phase conjugation by direct SBS, this process does not have a threshold intensity for the incident probe wave. However, the SBS threshold must still be exceeded in the cell by a strong incident pump wave before the nonlinear medium becomes an effective conjugator.

Here, we consider a new technique of Brillouin-induced phase conjugation. It employs the strong Brillouin resonant enhancement of near-degenerate four wave mixing, but is a parametric process with no threshold. We show that resonant conjugate reflectivity occurs at four distinct frequencies corresponding to the Stokes and anti-Stokes frequencies at two distinct Brillouin shifts. By controlling the polarization states of pump and probe waves, we can arbitrarily choose the Brillouin resonance contributing to the reflectivity, and suppress the other. Finally, we state briefly the limitations of the fidelity of this conjugation process due to the difference in frequency between the input object wave and the reflected conjugate wave.

Consider the optical fields incident on the sample shown in Fig. 5.1. Two counterpropagating pump waves of the same frequency Ω but arbitrary polarizations are incident on the sample, propagating to the right and left along the z-axis. A third weak probe wave at ω interrogates the sample, travelling obliquely in the y-z plane parallel to $\hat{s}$. The pump and probe waves are given by:

$$\vec{E}_R(z,t) = \tfrac{1}{2}\hat{e}_R\mathcal{E}_R \exp i(Kz - \Omega t) + \text{c.c.} \tag{5.1}$$

$$\vec{E}_L(z,t) = \tfrac{1}{2}\hat{e}_L\mathcal{E}_L \exp i(-Kz - \Omega t) + \text{c.c.} \tag{5.2}$$

$$\vec{E}_P(\vec{r},t) = \tfrac{1}{2}\hat{e}_P \mathcal{E}_P \exp i(ks - \omega t) + \text{c.c.}, \tag{5.3}$$

where

$$\hat{s} = \hat{y}\sin\theta + \hat{z}\cos\theta \tag{5.4}$$

and $\hat{e}_R$, $\hat{e}_L$ and $\hat{e}_P$ are complex polarization vectors. We wish to consider the generation of a wave in the $-\vec{k}$ direction by nonlinear coupling of the pump and probe waves. The Fourier component of the nonlinear polarization giving rise to this wave is seen to be:

$$P_i^{(3)}(-\vec{k},\omega_4) = 6\chi_{ijk\ell}(-\vec{k} = -\vec{k} + \vec{K} - \vec{K};\ \omega_4 = -\omega + \Omega + \Omega)$$

$$\times\ [\mathcal{E}_P^* \mathcal{E}_R \mathcal{E}_L e_{Pj}^* e_{Rk} e_{L\ell}]. \tag{5.5}$$

Thus a new wave of frequency $\omega_4 = 2\Omega - \omega$ and wavevector $-\vec{k}$ is generated. Neglecting effects on the object and conjugate waves of either pump beam acting alone, the small signal behavior of the conjugate wave signal is given by the four wave mixing theory of Sec. 2.2. Writing the conjugate wave

$$\vec{E}_c(\vec{r},t) = \mathcal{E}_c(s)e^{-i(ks+\omega_4 t)} \tag{5.6}$$

the slow-wave approximation yields the equation

$$\frac{\partial \mathcal{E}_{ci}}{\partial s} = -\,i\,\frac{12\pi\omega_4}{nc}\,\chi_{eff}^{(3)}\mathcal{E}_R\mathcal{E}_L\mathcal{E}_P^* \exp\,(i\Delta ks) \tag{5.7}$$

where

$$\chi^{(3)}_{eff} = \chi_{ijk\ell}(-k;\omega_4)\, e_{Pj} e_{Rk} e_{L\ell} \tag{5.8}$$

and

$$\Delta k = 2\,\frac{n}{c}\,(\Omega - \omega). \tag{5.9}$$

If the effective overlap of the object wave with the two pump waves is L, then (5.7) predicts a conjugate wave intensity

$$I_c = \frac{nc}{8\pi}\,|\mathcal{E}_{ci}(L)|^2 = \left(\frac{96\pi^2\omega_4}{n^2c^2}\right)^2 L^2 |\chi^{(3)}_{eff}|^2 I_P I_R I_L\,\frac{\sin^2(\Delta kL/2)}{(\Delta kL/2)^2}\,. \tag{5.10}$$

Equation (5.10) is the generalization of the conjugate wave generation process, when pump and probe are detuned, for any mechanism contributing to $\chi^{(3)}_{eff}$. We see that the process will only be effective over a coherence length

$$L_{coh} \approx \pi/\Delta k = \frac{1}{4n\Delta\bar{\nu}}\ \text{cm} \tag{5.11}$$

where $\Delta\bar{\nu}$ is the pump-probe detuning expressed in units of wavenumbers. Equation (5.11) predicts a coherence length of 6.7 mm for $\Delta\bar{\nu} = .23\ \text{cm}^{-1}$, the largest Brillouin shift in CS_2 at $\omega \approx 17000\ \text{cm}^{-1}$. From experience in observing coherent Brillouin signals with much shorter overlap lengths, we already know that this Brillouin conjugation process will be observable for laser intensities below the thresholds for SBS.

We now consider the dispersion and tensor properties of the suscep-

tibility, as applied to this process in CS_2. We need only evaluate Eqs. (1.36), (1.47), and (1.53) to obtain the orientational, Brillouin, and electronic contributions to $\chi^{(3)}(-\vec{k} = -\vec{k} + \vec{K} - \vec{K};\ \omega_4 = -\omega + \Omega + \Omega)$. We obtain

$$\chi_{1122} = \frac{1}{24}\left[\frac{2b(0)}{1 - i\Delta\tau} + \sigma\right] \tag{5.12a}$$

$$\chi_{1221} = \frac{1}{24}\left[\frac{1}{3}\frac{b(0)}{1 - i\Delta\tau} + \sigma\right] + B\,\frac{\omega_{B1}^2}{\omega_{B1}^2 - \Delta^2 - 2i\Gamma_1\Delta} \tag{5.12b}$$

$$\chi_{1212} = \frac{1}{24}\left[\frac{1}{3}\frac{b(0)}{1 - i\Delta\tau} + \sigma\right] + B\,\frac{\omega_{B2}^2}{\omega_{B2}^2 - \Delta^2 - 2i\Gamma_2\Delta} \tag{5.12c}$$

where $B = \gamma^2/384\pi^2\rho_o v^2$, $\Delta = \Omega - \omega$, and the two distinct Brillouin shifts are

$$\omega_{B1} = v|-\vec{k} + \vec{K}| = \frac{2n\Omega v}{c}\sin(\theta/2) \tag{5.13}$$

$$\omega_{B2} = v|-\vec{k} - \vec{K}| = \frac{2n\Omega v}{c}\cos(\theta/2). \tag{5.14}$$

Γ_1 and Γ_2 allow for different damping constants for the acoustic phonons of wavevectors $\vec{q}_1 = -\vec{k} + \vec{K}$ and $\vec{q}_2 = -\vec{k} - \vec{K}$, respectively.

Note the differing Brillouin contributions for the three tensor components of $\chi^{(3)}$. As expected, there is no acoustic phonon resonance in χ_{1122}; this element governs the completely depolarized conjugate wave generation and contains only electronic and orientational contributions. More striking is how the two other elements "pick out" resonances at distinct Brillouin shifts. Referring to Eqs. (5.12b) and (5.12c) and Fig. 5.2, we clearly see how χ_{1221} is related to the excitation of phon-

on $\vec{q}_1$ since this term governs the coupling of the parallel polarized components of the probe and right-going pump waves. χ_{1212} and $\vec{q}_2$ are similarly related. We note that at exact degeneracy, $\Delta = \Omega - \omega = 0$, static electrostriction produces two non-propagating density gratings in the medium by interaction of the probe beam with the pump beams. Each grating then elastically diffracts the opposite beam into the conjugate direction. Similar gratings of excited state population or molecular orientation govern the already observed conjugate wave generation due to electronic excitation[77,88-90] and the optical Kerr effect.[75,76]

To demonstrate the tuning and polarization properties of this "Brillouin mirror" we may adopt the geometry of Fig. 5.1. Suppose that the probe beam is polarized along $\hat{x}$, $\hat{e}_P = \hat{x}$. Let the right-going wave also be polarized along $\hat{x}$, $\hat{e}_R = \hat{x}$, and adjust the slow axis of the quarter-wave plate to be at 45° to $\hat{x}$. Then $\hat{e}_L = \hat{y}$, $\chi^{(3)}_{eff} = \chi_{1221}$, and only the Brillouin peaks corresponding to ω_{B1} contribute to the resonant four wave mixing. If $\hat{e}_P$ remains $\hat{x}$, we rotate $\hat{e}_R$ to $\hat{y}$, the $\lambda/4$ plate produces $\hat{e}_L = \hat{x}$, and $\chi^{(3)}_{eff} = \chi_{1212}$. Now the Stokes and anti-Stokes peaks at $\Delta = \omega_{B2}$ produce the resonant generation. If both pump beams are polarized at 45° to $\hat{x}$ and the probe is along $\hat{x}$, both sets of peaks are present. Finally, if the pump and probe beams are polarized orthogonally, only the orientational and electronic contributions are present. Note, however, that this is <u>not</u> a good way to do Rayleigh-wing spectroscopy because coherence lengths will now seriously limit the tuning range due to phase mismatch.

We have made a calculation of the expected phase conjugate reflectivity $R_c = I_c/I_p$. We consider two uniform plane wave beams, square in cross section, with area 9 mm^2, intersecting at an angle $\theta = \sin^{-1} 3/5 =$

36.9°. The frequency is 17000 cm^{-1}. The Brillouin shifts are 2.19 and 6.58 GHz, so the four peaks appear equally spaced. The overlap length is 5 mm. It is desirable that the pump beams produce negligible Brillouin gain to reduce ambiguity. From Eq. (2.24a) and a peak (backward) Brillouin susceptibility 6.5×10^{-12} esu, we compute a gain of .167 cm/MW, in good agreement with tabulated values.[10] If the cell is of length 1 cm, we should use 50 kW in the 9 mm^2 beams to reduce the Brillouin gain to 10%. We assume near-transform limited pulses giving an effective phonon linewidth (FWHM) of 200 MHz. The peak susceptibilities for the ω_{B1} mode (χ_{1221}) and the ω_{B2} mode (χ_{1212}) are then 7.3×10^{-13} esu and 2.2×10^{-12} esu, the difference arising because the peak susceptibilities are proportional to the Brillouin shifts. For the narrow band lasers, the other contributions to the susceptibility are negligible. We obtain, for these conditions, $R_1 = 6.5 \times 10^{-6}$ and $R_2 = 4.0 \times 10^{-5}$ for the conjugate reflectivities for the ω_{B1} and ω_{B2} modes. The resonance curves are sketched in Fig. 5.3. We expect that for 9 mm^2 beams, the CS_2 cell can withstand at least two orders of magnitude more pump intensity before the onset of self-focusing or stimulated Brillouin oscillation.[76] Then, reflectivities on the order of unity should be observed, but our small signal treatment would have to be modified.

From Fig. 5.3 we see that the parametric "Brillouin mirror" can act as a polarization and spatial (angular) filter. The free spectral range is of order $2\omega_B$ and the resolution is of order 100 MHz. To achieve high reflectivities requires a relatively high power, narrow band laser, a disadvantage when compared to using atomic vapor to construct a similar filter.[91] However, the Brillouin mirror described here will work at any visible frequency, does not require coincidence with an atomic resonance

line, and has comparable resolution.

To close, we mention briefly to what extent the fidelity of the conjugation process is affected by the frequency shift of $2\omega_B$ between image and object waves. Hellwarth[73] shows that we may expect a slight magnification or demagnification equal to $[1 \pm 2\omega_B/\omega_{LIGHT}]$ for Stokes or anti-Stokes generation, respectively. We also see that in retraversing a phase aberration $2\pi(\Delta ns)/\lambda$, the conjugate wave fails to correct for the aberration by the same factor $[1 \pm 2\omega_B/\omega_{LIGHT}]$. Since $2\omega_B/\omega_L \approx 3 \times 10^{-5}$, we see that using the Brillouin resonance for phase conjugation incurs very little penalty in fidelity.

Figure Captions

Fig. 5.1 Experimental geometry and field definition in Brillouin-induced phase conjugation.

Fig. 5.2 Relationship of wavevectors of pump waves, probe wave, and excited phonons.

Fig. 5.3 Brillouin-induced phase conjugate reflectivity for two different pump polarization configurations.

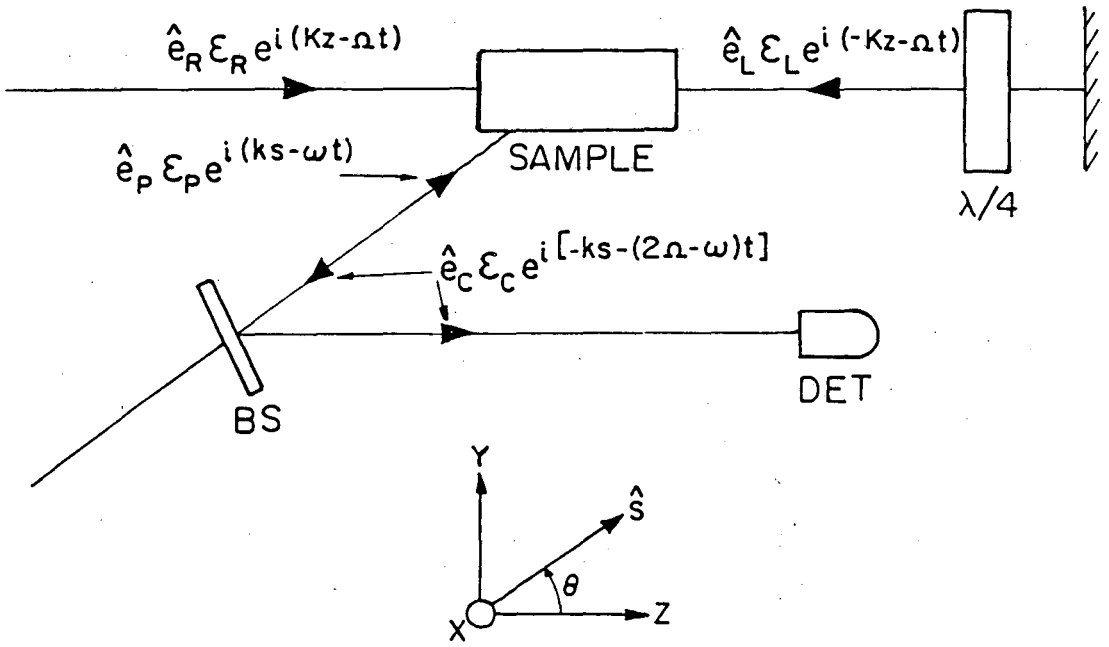

Figure 5.1

XBL823-5345

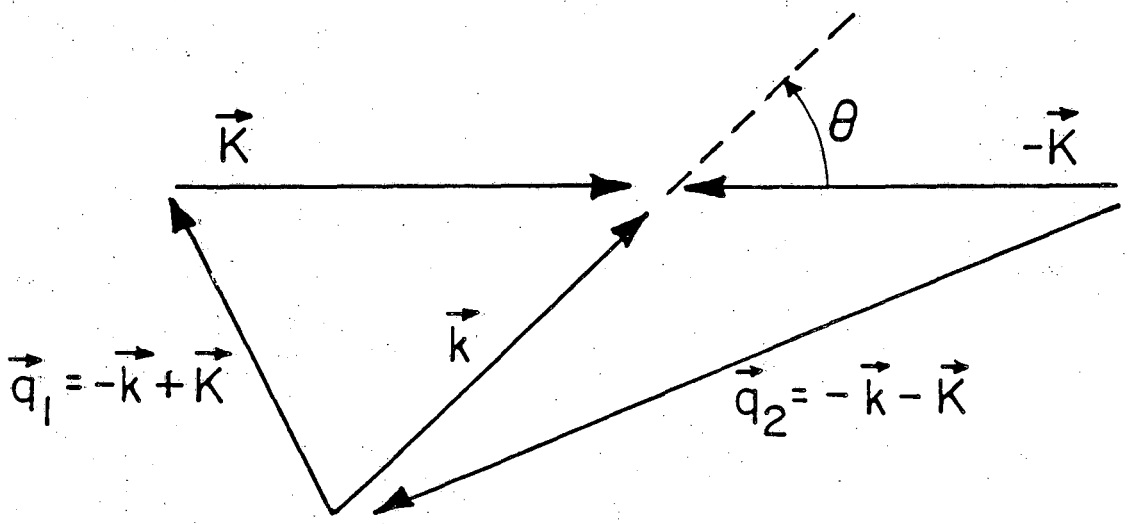

XBL 823-5346

Figure 5.2

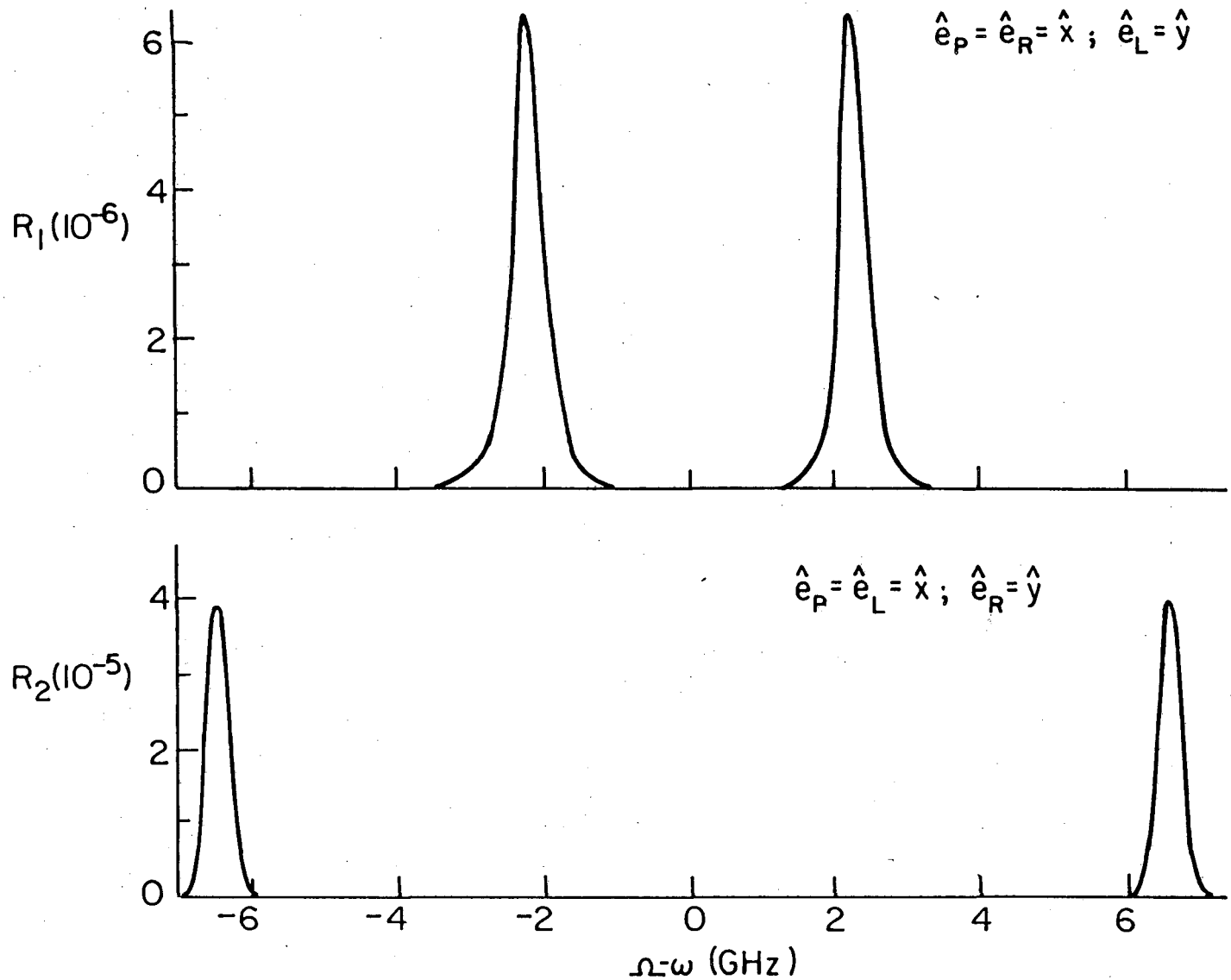

Figure 5.3

XBL 823-5347

References

1. J. A. Armstrong, N. Bloembergen, J. Ducuing, and P. S. Pershan, Phys. Rev. 127, 1918 (1962).
2. F. Gires and G. Mayer, Compt. Rend. 258, 2039 (1964).
3. P. D. Maker, R. W. Terhune, and C. M. Savage, Phys. Rev. Lett. 12, 507 (1964).
4. G. Askaryan, Sov. Phys. JETP 15, 1088 (1962).
5. R. Y. Chiao, C. H. Townes, and B. P. Stoicheff, Phys. Rev. Lett. 12, 592 (1964).
6. D. I. Mash, V. V. Morozov, V. S. Starunov, and I. L. Fabelinskii, JETP Lett. 2, 25 (1965).
7. N. Bloembergen and P. Lallemand, Phys. Rev. Lett. 16, 81 (1966).
8. R. Y. Chiao, Brillouin Scattering and Coherent Phonon Generation (Ph.D. thesis, M.I.T., unpublished, 1965).
9. Y. R. Shen, Phys. Rev. Lett. 20, 378 (1966).
10. W. Kaiser and M. Maier, in Laser Handbook, ed. by F. T. Arrechi and E. O. Schulz-Dubois (North-Holland, Amsterdam, 1972).
11. P. D. Maker and R. W. Terhune, Phys. Rev. 137, A801 (1965).
12. Paul N. Butcher, Nonlinear Optical Phenomena (Bulletin 200, Engineering Experiment Station, Ohio State University, Columbus, 1965).
13. Harold Jeffries, Cartesian Tensors (Cambridge University Press, Cambridge, 1952).
14. Adelbert Owyoung, The Origins of the Nonlinear Refractive Indices of Liquids and Glasses (Ph.D. thesis, Calif. Inst. of Tech., unpublished, 1971).
15. R. Y. Chiao and J. Godine, Phys. Rev. 185, 430 (1969).

16. E. G. Hanson, Nonlinear Optical Effects in Liquid Crystals (Ph.D. thesis, Lawrence Berkeley Lab. Report LBL-6022, 1976).

17. P. Debye, Polar Molecules (Dover Publications, New York, 1945).

18. R. W. Hellwarth, Prog. Quant. Electr. 5, 1 (1977).

19. W. K. H. Panofsky and M. Phillips, Classical Electricity and Magnetism (Addison-Wesley, Reading, 1955).

20. D. A. Kleinman, Phys. Rev. 126, 1977 (1962).

21. M. D. Levenson and N. Bloembergen, Phys. Rev. B 10, 4447 (1974).

22. R. T. Lynch, M. D. Levenson, and N. Bloembergen, Phys. Lett. 50A, 61 (1974).

23. H. Lotem and R. T. Lynch, Phys. Rev. Lett. 37, 334 (1976); also see R. T. Lynch and H. Lotem, J. Chem. Phys. 66, 1905 (1977).

24. A. Owyoung, Opt. Commun. 16, 266 (1976).

25. E. A. Volkova, V. A. Zamkov, and L. V. Nalbandov, Opt. Spectrosc. 30, 300 (1971).

26. J. J. Song and M. D. Levenson, J. Appl. Phys. 48, 3496 (1977).

27. Y. Kato and G. A. Zdasiuk, J. Opt. Soc. Am. 65, 995 (1975).

28. Y. Kato and B. P. Stoicheff, Phys. Rev. B 11, 3984 (1975).

29. M. D. Levenson, Physics Today 30, 44 (1977) and references therein.

30. M. D. Levenson and J. J. Song, "Coherent Raman Spectroscopy," in Coherent Nonlinear Optics, V. 21 in Topics in Current Physics (Springer-Verlag, Berlin, 1980).

31. R. W. Smith, Wave Mixing Spectroscopy (Ph.D. thesis, Lawrence Berkeley Lab. Report LBL-11518, 1980).

32. R. F. Begley, A. B. Harvey, and R. L. Beyer, Appl. Phys. Lett. 25, 387 (1974).

33. R. J. Hall, J. A. Shirley, and A. C. Eckbreth, Opt. Lett. 4, 87

(1979).

34. J. W. Nibler, J. R. McDonald, and A. B. Harvey, Opt. Commun. 18, 371 (1976).

35. See Laser Focus 15, 32 (1979).

36. A. C. Eckbreth, Appl. Phys. Lett. 32, 421 (1978).

37. S. Chandra, A. Compaan, and E. Wiener-Avnear, Appl. Phys. Lett. 33, 867 (1978).

38. A. Compaan and S. Chandra, Opt. Lett. 4, 170 (1979).

39. S. A. Akhmanov, A. F. Bunkin, S. G. Ivanov, and N. I. Koroteev, Sov. Phys. JETP 47, 667 (1978).

40. J-L. Oudar, R. W. Smith, and Y. R. Shen, Appl. Phys. Lett. 34, 758 (1979).

41. L. A. Rahn, L. J. Zych, and P. L. Mattern, Opt. Commun. 30, 249 (1979).

42. J. J. Song, G. L. Eesley, and M. D. Levenson, Appl. Phys. Lett. 29, 567 (1976).

43. W. J. Jones and B. P. Stoicheff, Phys. Rev. Lett. 13, 657 (1964).

44. A. Owyoung and E. D. Jones, Opt. Lett. 1, 152 (1977).

45. A. Owyoung, Opt. Commun. 22, 323 (1977).

46. A. Owyoung, IEEE J. Quant. Elect. QE-14, 192 (1978).

47. A. Yariv, Introduction to Optical Electronics (Holt, Rinehart, and Winston, New York, 1971).

48. A. Owyoung, CW Stimulated Raman Spectroscopy, in Chemical Applications of Nonlinear Spectroscopy, A. Harvey, ed. (Academic Press, New York, 1978).

49. A. Owyoung, Opt. Lett. 2, 91 (1978).

50. D. Heiman, R. W. Hellwarth, M. D. Levenson, and G. Martin, Phys.

Rev. Lett. 36, 189 (1976).

51. G. L. Eesley, M. D. Levenson, and J. J. Song, IEEE J. Quant. Elect. QE-13, 31D (1977).

52. G. L. Eesley, M. D. Levenson, and W. M. Tolles, IEEE J. Quant. Elect. QE-14, 45 (1978).

53. M. D. Levenson and G. L. Eesley, Appl. Phys. 19, 1 (1979).

54. B. W. Woodward, V. J. Ehlers, and W. C. Lineberger, Rev. Sci. Instr. 44, 882 (1973).

55. D. A. Leonard, Appl. Phys. Lett. 7, 4 (1965).

56. W. A. Fitzsimmons, L. W. Anderson, C. E. Reidhauser, and J. M. Vrtilek, IEEE J. Quant. Elect. QE-12, 624 (1976).

57. A. W. Ali, A. C. Kolb, and A. W. Anderson, Appl. Opt. 6, 2115 (1976).

58. R. Targ, IEEE J. Quant. Elect. QE-8, 726 (1972).

59. J. Levatter and S-C. Lin, Appl. Phys. Lett. 25, 703 (1974).

60. M. Geller, D. E. Altman, and T. A. Detemple, Appl. Opt. 7, 2232 (1968).

61. S. Chu, Ph.D. thesis (Lawrence Berkeley Laboratory Report LBL-5731, 1976).

62. T. W. Hänsch, Appl. Opt. 11, 895 (1972).

63. R. Wallenstein and T. W. Hänsch, Opt. Commun. 14, 353 (1975).

64. R. Wallenstein and T. W. Hänsch, Appl. Opt. 13, 1625 (1974).

65. M. D. Levenson and J. J. Song, private communication.

66. S. L. Shapiro and H. P. Broida, Phys. Rev. 154, 129 (1967).

67. E. P. Ippen and C. V. Shank, Appl. Phys. Lett. 26, 92 (1975).

68. M. A. F. Scarparo, J. H. Lee, and J. J. Song, Opt. Lett. 6, 193 (1981).

69. See also R. Y. Chiao and J. Godine, Phys. Rev. 185, 430 (1969).

70. Reference 14, section 4.2.3.

71. J. G. Skinner and W. G. Nilsen, J.O.S.A. 58, 113 (1968).

72. Y. Kato and H. Takuma, J.O.S.A. 61, 347 (1971).

73. R. W. Hellwarth, J.O.S.A. 67, 1 (1977)

74. A. Yariv and D. Pepper, Opt. Lett. 1, 16 (1977).

75. D. M. Bloom and G. C. Bjorklund, Appl. Phys. Lett. 31, 592 (1977).

76. S. M. Jensen and R. W. Hellwarth, Appl. Phys. Lett. 32, 166 (1978).

77. D. M. Bloom, P. F. Liao, and N. P. Economou, Opt. Lett. 2, 58 (1978).

78. D. M. Pepper, D. Fekete, and A. Yariv, Appl. Phys. Lett. 33, 41 (1978).

79. B. Ya Zel'dovich, V. I. Popovichev, V. V. Ragul'skii, and F. S. Faizullov, JETP Lett. 15, 109 (1972).

80. I. M. Bel'dyugin, M. G. Galushkin, E. M. Zemskov, and V. I. Mandrosov, Sov. J. Quant. Elect. 6, 1349 (1977).

81. B. Ya Zel'dovich, N. F. Filipetskii, V. V. Ragul'skii, and V. V. Shkunov, Sov. J. Quant. Elect. 8, 1021 (1978), and references therein.

82. O. Yu Nosach, V. I. Popovichev, V. V. Ragul'skii, and F. S. Faizullov, JETP Lett. 16, 435 (1972).

83. V. Wang and C. R. Giuliano, Opt. Lett. 2, 4 (1977).

84. N. Basov and I. Zubarev, Appl. Phys. 20, 261 (1979).

85. N. G. Basov, I. G. Zubarev, A. V. Kotov, S. I. Mikhailov, and M. G. Smirnov, Sov. J. Quant. Elect. 9, 237 (1979).

86. I. M. Bel'dyugin, E. M. Zemskov, and V. N. Klushin, Sov. J. Quant. Elect. 9, 1200 (1979).

87. R. L. Abrams, C. R. Giuliano, and J. F. Lam, Opt. Lett. 6, 131 (1981).

88. R. L. Abrams and R. C. Lind, Opt. Lett. 2, 94 (1978). Errata Opt. Lett. 3, 205 (1979).

89. P. F. Liao and D. M. Bloom, Opt. Lett. 3, 4 (1978).

90. D. S. Hamilton, D. Heiman, Jack Feinberg, and R. W. Hellwarth, Opt. Lett. 4, 124 (1979).

91. J. Nilsen, N. Gluck, and A. Yariv, Opt. Lett. 6, 380 (1981).

This report was done with support from the Department of Energy. Any conclusions or opinions expressed in this report represent solely those of the author(s) and not necessarily those of The Regents of the University of California, the Lawrence Berkeley Laboratory or the Department of Energy.

Reference to a company or product name does not imply approval or recommendation of the product by the University of California or the U.S. Department of Energy to the exclusion of others that may be suitable.

TECHNICAL INFORMATION DEPARTMENT
LAWRENCE BERKELEY LABORATORY
UNIVERSITY OF CALIFORNIA
BERKELEY, CALIFORNIA 94720